minerals

IMPACT FACTOR 2.2

CITESCORE 4.1

Article

From Source to Sink: U-Pb Geochronology and Lithochemistry Unraveling the Missing Link Between Mesoarchean Anatexis and Magmatism in the Carajás Province, Brazil

Marco Antônio Delinardo-Silva, Lena Virgínia Soares Monteiro, Carolina Penteado Natividade Moreto, Jackeline Faustinoni, Ticiano José Saraiva Santos, Soraya Damasceno Sousa and Roberto Perez Xavier

Special Issue

Geochemistry and Geochronology of High-Grade Metamorphic Rocks

Edited by

Dr. Zhuang Li, Dr. Zhanzhan Duan, Dr. Ting Liu and Dr. Hafiz U. Rehman

MDPI

https://doi.org/10.3390/min15030265

minerals

MDPI

Article

From Source to Sink: U-Pb Geochronology and Lithochemistry Unraveling the Missing Link Between Mesoarchean Anatexis and Magmatism in the Carajás Province, Brazil

Marco Antônio Delinardo-Silva [1], Lena Virgínia Soares Monteiro [2,*], Carolina Penteado Natividade Moreto [3], Jackeline Faustinoni [3], Ticiano José Saraiva Santos [3], Soraya Damasceno Sousa [4] and Roberto Perez Xavier [3,5]

[1] Geography, Geosciences and Public Health Institute, University of Uberlândia, Uberlândia 38408-100, Brazil; marco.delinardo@ufu.br
[2] Geoscience Institute, University of São Paulo, São Paulo 05508-080, Brazil
[3] Geoscience Institute, University of Campinas, Campinas 13083-855, Brazil; cmoreto@unicamp.br (C.P.N.M.); jfaustinoni@gmail.com (J.F.); ticiano@unicamp.br (T.J.S.S.); roberto.xavier@adimb.org.br (R.P.X.)
[4] National Institute of Industrial Property, Rio de Janeiro 20090-910, Brazil; sorayadsousa@gmail.com
[5] Agency for the Development and Innovation of the Brazilian Mineral Sector, Brasilia 70712-903, Brazil
* Correspondence: lena.monteiro@usp.br

Abstract: The connection between crustal anatexis and magmatism is key to understanding the mechanisms that drive the evolution of the continental crust. Isotope geology and lithochemistry are important tools for reconstructing links between these processes, as field evidence of their connection is often obliterated by deformation in high-grade terrains. Thus, this study proposes new insights into the connection between the Mesoarchean regional metamorphism, crustal anatexis, and plutonism in the northern sector of the Carajás Province (i.e., Carajás Domain), in the Amazonian Craton, around 2.89 to 2.83 Ga. The widespread crustal anatexis in the Carajás Domain involved the water-fluxed melting of banded orthogneisses of the Xingu Complex and Xicrim-Cateté Orthogranulite (crystallization age at ca. 3.06–2.93 Ga), producing metatexites and diatexites with stromatic, net, schollen, and schlieren morphologies and coeval syntectonic leucosomes with composition similar to tonalites, trondhjemites, and granites. These leucosomes yielded crystallization ages of 2853 ± 5 Ma (MSWD: 0.61), 2862 ± 13 Ma (MSWD: 0.1), and 2867 ± 7 Ma (MSWD: 1.3). Their lithochemical data are similar to those of several diachronous Mesoarchean granitoids of the Carajás Domain in terms of major, minor, and trace elements and magmatic affinity. In addition, binary log–log vector diagrams (e.g., La vs. Yb; Rb vs. Yb), Sr/Y vs. Y, and Eu/Eu* vs. Yb plots indicate that plagioclase fractionation preceded melt extraction, establishing evolving source-to-sink trends between leucosomes and granites. These results show that the interplay between high-grade metamorphism, crustal anatexis, and magmatism may have shaped the evolution of the Mesoarchean continental crust in the Carajás Province, developing a petrotectonic assemblage associated with collisional orogens. The Mesoarchean geodynamic setting played a critical role in the development of coeval ca. 2.89 Ga magmatic–hydrothermal copper deposits in the Carajás Province, as well as Neoarchean world-class iron oxide–copper–gold deposits linked to post-orogenic extensional rebound.

Keywords: crustal evolution; Carajás Province; partial melting; granitoids

Academic Editors: Giorgio Garuti, Zhuang Li, Zhanzhan Duan, Ting Liu and Hafiz U. Rehman

Received: 7 January 2025
Revised: 23 February 2025
Accepted: 26 February 2025
Published: 3 March 2025

Citation: Delinardo-Silva, M.A.; Monteiro, L.V.S.; Moreto, C.P.N.; Faustinoni, J.; Santos, T.J.S.; Sousa, S.D.; Xavier, R.P. From Source to Sink: U-Pb Geochronology and Lithochemistry Unraveling the Missing Link Between Mesoarchean Anatexis and Magmatism in the Carajás Province, Brazil. *Minerals* **2025**, *15*, 265. https://doi.org/10.3390/min15030265

1. Introduction

Partial melting, anatectic liquid extraction, and its ascent configure an efficient chemical differentiation of the continental crust, leaving a more refractory and gradually more mafic residue at its base while feeding its upper portion with the expelled felsic component [1,2]. In this context of crustal reworking, migmatites and granulites record pervasive partial melting, melt loss, and melt transfer through the lower and middle crust [1,2]. The accumulations of anatectic melts compositionally modified by contamination (e.g., interactions with restite, wall rocks, or different magmas) and fractional crystallization will determine the composition of granitoids in the upper crust [1,2].

The migration and emplacement of melts can be traced in the field in some large migmatite, granulite, and granite complexes worldwide (e.g., [3–5]). However, in Archean poly-deformed terrains, the stratigraphic relationship between the components of these complexes cannot be easily reconstructed (e.g., [6]). In these cases, the characterization of the geochemical composition of leucosomes and granitoids, combined with U-Pb geochronology, helps to determine the sequence of partial melting events and explore the possible connection between these two components (e.g., [7,8]).

The Carajás Province, a major metallogenic province in the Amazonian Craton, has an ancient continental crust (ca. 3.06 to 2.93 Ga) generated by the partial melting of mafic granulites at the base of island arcs [9]. This crust was subsequently metamorphosed under upper amphibolite and granulite facies conditions and experienced partial melting in the Late Mesoarchean (ca. 2.89 to 2.84 Ga; [9–12]). Several elongated, variably deformed, chemically and isotopically diverse syntectonic granitoids were emplaced within ENE-to-WNW-trending ductile structures (e.g., gneissic foliation, shear zones; [13–20]) during this period. Most primary contacts between granitoids, migmatites, and orthogneisses were overprinted during the development of megashear zones (e.g., Canaã, Carajás, and Cinzento) in the context of Neoarchean transpressional and transtensional tectonics [19,20]. Thus, the link between metamorphism, partial melting, and magmatism remains unclear, challenging the definition of the geodynamic setting (drip tectonics vs. subduction–collisional models; [9,12,15,21,22]) related to the Mesoarchean crustal evolution.

This study provides petrological evidence of the partial melting processes in the Late Mesoarchean and the source-to-sink connection between the leucosomes of migmatites of the northern Carajás Province (i.e., Carajás Domain) and granitoids based on field, petrographic, lithochemical, and U-Pb geochronological data. It shows that the widespread partial melting of crustal lithotypes was synchronous with regional deformation and was influenced by the influx of water into a hot lower and middle crust. The short time span of approximately 50 Ma for metamorphism and partial melting (ca. 2.89 to 2.84 Ga), overlapping with mantle- and crustal-derived magmatism during a regional compressive context [19,20], favors a subduction-to-collision setting for the Carajás Province in the Late Mesoarchean. This geodynamic setting was critical for developing Mesoarchean–Neoarchean base metal mineral systems in the Amazonian Craton.

2. Geological Setting of the Carajás Province

The Carajás Province (Figure 1) is a large crustal block composed primarily of Archean rocks (ca. 3.0 to 2.7 Ga; [23,24]). It is located in the southeastern portion of the Amazonian Craton (Figure 1) and is surrounded by Siderian to Ediacaran units [23,24]. Santos [23] divided the province into the Carajás (North) and Rio Maria (South) domains (Figure 1). This subdivision was based on geochronological data, which initially suggested a dominance of Mesoarchean rocks in the Rio Maria Domain and its subordinate occurrence in the Carajás Domain [23,24]. However, the expansion of U-Pb geochronological data has shown that Mesoarchean rocks are also abundant in the Carajás Domain (e.g., [9,13–18,25]).

The Mesoarchean crust of the Rio Maria Domain is composed of greenstone belts, tonalite–trondhjemite–granodiorite (TTG), sanukitoids, and potassic granitoids, with ages ranging from ca. 3.04 to 2.86 Ga [26–28]. These authors suggested that the crustal evolution of the Rio Maria Domain involved subduction episodes and collisions between the crustal landmasses formed in accretionary orogens.

The Carajás Domain records episodes of crust formation and reworking, large basin formation and inversion, and intra-plate magmatism, spanning from the Mesoarchean to the Paleoproterozoic (ca. 3.06 to 1.88 Ga [9,10,12,13,15,17,19,20,25,29–32]). The origin of the continental crust of the Carajás Domain is also ascribed to subduction episodes, which formed the protoliths of the Orthogranulite Xicrim-Cateté and Xingu Complex, with crystallization ages of ca. 3.06 to 2.93 Ga (Figure 1; [9]), and resulted in the amalgamation of fragments of oceanic islands (greenstone belts) to the previous formed proto-continents [33].

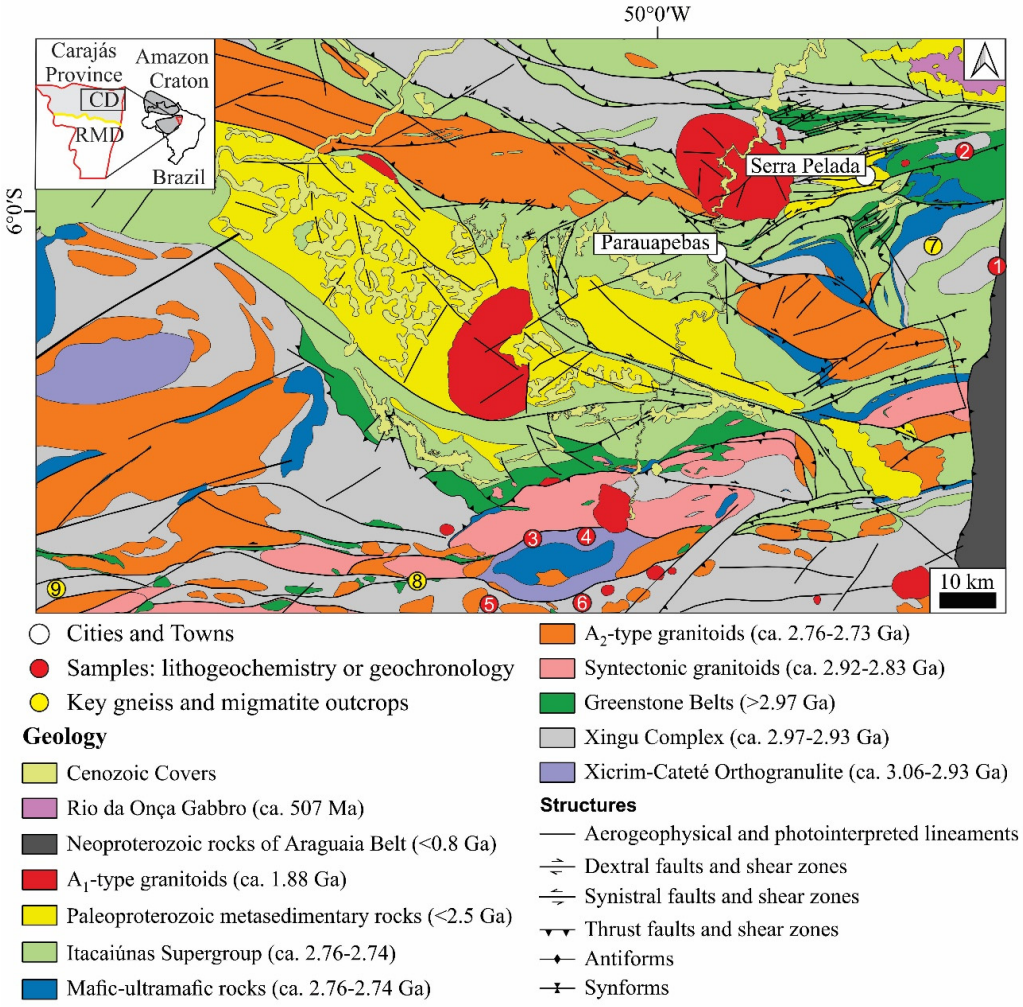

Figure 1. Geological map of the northern portion of the Carajás Province. The map highlights the position of the province in the Amazonian Craton and its subdivision into the Carajás (DC) and Rio Maria (RMD) domains, as shown in the inset figure in the upper right corner. Meaning of the numbers on the map: (1) Britamil quarry (lithochemistry samples: G1 to G7; J1 to J3; geochronology samples: G1 and J1; see the Figures 4C and 6A in the Section 4); (2) Britalider quarry (geochronology sample A1; see the Figure 4A,B in the Section 4); (3) lithochemistry sample location: SM36 L1 and L2 (see the Figure 2A in the Section 4) and SM41L; (4) lithochemistry sample location: SM39N; (5) lithochemistry sample location: XS37L (see the Figure 2E in the Section 4). Near key outcrop (see the Figure 6B in the Section 4); (6) lithochemistry sample location: XS24L (see the Figure 4D in the Section 4); (7) key outcrop (see the Figure 2B in the Section 4); (8) key outcrop (see the Figure 2D in the Section 4); (9) key outcrop (see the Figure 2C in the Section 4) (Modified from Costa et al. [34]).

The Xicrim-Cateté Orthogranulite comprises mafic granulites and diopside–enstatite orthogneisses with TTG compositions [9,20]. The mafic rocks have been interpreted as relicts of immature island arcs older than ca. 3.0 Ga [9]. The authors also suggested that, during the evolution of these arcs, the basic lower crust was partially melted, leading to the formation of the first fragments of felsic continental crust in the Carajás Domain. Incongruent melting produced the protoliths of the diopside–enstatite orthogneisses, which formed episodically between ca. 3.0 and 2.93 Ga [9].

The protoliths of the orthogneisses of the Xingu Complex include biotite- or hornblende-bearing granitoids of TTG composition, which form the middle crust component of the earliest continental fragments in the Carajás Domain [9]. The protoliths of these orthogneisses show crystallization ages of ca. 2.97 and 2.94 Ga [9,35]. The Lu-Hf and lithochemical data of the biotite and hornblende orthogneisses of the Xingu Complex and diopside–enstatite orthogneisses of the Xicrim-Cateté Orthogranulite suggest a common source for their protoliths [9]. Other gneisses (e.g., Canaã dos Carajás Granite and Rio Verde Trondhjemite, ca. 2.95–2.93 Ga; [13]) and foliated to isotropic granites and tonalites (e.g., Sequeirinho Granite and Bacaba Tonalite, ca. 3.01–2.99 Ga; [25,36]) also contribute to the formation of the continental crust of the Carajás Domain, but their relationship with the orthogneisses protoliths is unknown.

The continental crust of the Carajás Domain formed at ca. 3.06–2.93 Ga was metamorphosed and partially melted between ca. 2.89 and 2.84 Ga [9–12], synchronous to the development of an ENE-to-WNW ductile fabric in the ancient basement rocks [19,20]. This regional metamorphic and deformational event was responsible for the second record of an anatectic event of the Xicrim-Cateté Orthogranulite and the first record of an anatectic event of the Xingu Complex [9,10]. Several elongate syntectonic granites (Figure 1) were emplaced previously and during this metamorphic and deformational event at ca. 2.92 to 2.83 Ga (e.g., Campina Verde Tonalitic Complex, Serra Dourada Granite, Agua Limpa Suite, Nova Canada Leucogranite; Ourilândia Plutonic Complex; [13,15,17,18]). These granitoids are chemically and isotopically diverse, comprising TTG and sanukitoids (ca. 2.92–2.84 Ga), interpreted as slab- or mantle-derived melts (εNd: +2.75; εHf: −1.0 to +3.2), as well as calc-alkaline to alkaline granitoids (ca. 2.88–2.83 Ga), understood to be crustal melts (εNd: −8.3 to +2.4; εHf: −4.1 to +1.2; [13,15,17,18]).

After approximately 70 Ma of tectonic quiescence, the northern portion of the Carajás Domain experienced an extensional event [19], which culminated in predominantly basaltic volcanism and the deposition of thick banded iron formations (BIFs), and volcaniclastic and siliciclastic units of the volcano-sedimentary Itacaiúnas Supergroup (Figure 1) between ca. 2.77 and 2.73 Ga [10,37]. The Itacaiúnas Supergroup extends over 300 km along the east–west strike of the Carajás Basin. Synchronous A_2-type granites (e.g., Estrela Granite complex; [32]) and layered mafic–ultramafic intrusions (e.g., Luanga; [10]; Figure 1) were also related to this Neoarchean striking magmatic event in the Carajás Domain, which has been correlated to a large igneous province (LIP) by Siepierski and Ferreira Filho [38], named as Parauapebas LIP [39].

During the Ryacian (ca. 2.2–2.0 Ga), the juvenile crust of the Bacajá Domain was amalgamated with the northern portion of the Carajás Domain, leading to the reactivation of shear zones in the latter [40–42]. Isotropic A_1-type granites with typical rapakivi textures intruded the Carajás and Rio Maria domains in the Orosirian (ca. 1.88 Ga; [43]). In the Neoproterozoic, the eastern border of the Carajás Province was reworked due to the development of the Araguaia Belt [41,44]. In this context, the emplacement of the Rio da Onça Gabbro (ca. 507 Ma; Figure 1) may reflect the last tectono-thermal event in the Carajás Province, which was related to the post-collisional history of this orogenic belt [45].

The Carajás Province is one of the world's major metallogenic provinces, known for its BIF-hosted iron ore, manganese, nickel, and copper–gold. The province includes ca. 2.89 Ga magmatic–hydrothermal copper deposits (e.g., Hades and Hades NE; [46]) and one of the largest known concentrations of word-class iron oxide–copper–gold (IOCG) deposits, formed during the Neoarchean (ca. 2.71–2.68 Ga and ca. 2.57 Ga) and Paleoproterozoic (ca. 1.88 Ga; [36,47]). The IOCG deposits are spatially related to regional-scale alkaline hydrothermal alteration (e.g., albite, scapolite; [48]) within ENE-WNW-trending megashear zones (e.g., Canaã and Cinzento).

3. Analytical Procedures

3.1. Geochemistry

The sample selection focused on rocks without evidence of hydrothermal alteration. The neosome and paleosome parts of the migmatite were carefully separated to avoid contamination. Sixteen leucosome samples (n = 16) were prepared in the Geochemistry Laboratory at the University of Campinas (UNICAMP). Between 0.5 and 1.0 kg of each leucosome sample was crushed using a jaw crusher and then powdered using ring and planetary agate mills. Six of these samples were sent for analysis at Acme Labs, Canada. At the facility, major and minor elements were analyzed using inductively coupled plasma emission spectrometry (ICP–ES), and trace elements were analyzed using inductively coupled plasma mass spectrometry (ICP–MS).

Ten samples were analyzed in the Geochemistry Laboratory at UNICAMP. Major elements were determined by X-ray fluorescence (XRF) following the method proposed by Vendemiatto and Enzweiller [49], using a Philips PW2404 X-ray fluorescence spectrometer. Trace elements were measured by ICP-MS at the Isotope Geology Laboratory at UNICAMP, as described by Navarro et al. [50], using an Inductively Coupled Plasma-Mass Spectrometer X Series II (Thermo) equipped with collision cell technology (CCT).

The analysis of the lithochemical data and the creation of diagrams were performed using electronic spreadsheets and the software GCDkit (ver. 6.2.0; [51]). The mineral vectors were modeled using the following fractional crystallization equation: $C_L/C_0 = F^{(D-1)}$. D values for plagioclase, K-feldspar, amphibole, and biotite were extracted from Brophy et al. [52], Ewart and Griffin [53], and Nash and Crecraft [54].

3.2. U-Pb Geochronology

A set of four samples was selected for LA-ICP-MS U-Pb zircon geochronology. Samples were crushed and ground in a jaw crusher. Heavy minerals, including zircon, were concentrated using conventional gravity and magnetic techniques. The least magnetic zircon grains were hand-picked under a binocular microscope, mounted in epoxy blocks, and polished for exposing central sections. Cathodoluminescence (CL) and secondary electron (SE) imaging were performed for grain analysis and targeting. CL conditions were as follows: accelerating voltage of 15 kV, work distance of 16 mm, and emission current varying from 3000 pA to 8000 pA. The isotopic data acquisition was carried out at the Isotope Geology Laboratory at the UNICAMP (Campinas, Brazil) using a Thermo Fisher Element XR sector field ICP-MS and a Photon Machine Excite 193 nm ultra-short pulse excimer laser ablation system (Analyte Excite WH) with a HelEx 2 volume cell. Laser conditions were as follows: spot size of 25 µm, frequency of 10 Hz, and laser fluence of 4.7 J/cm^2. Zircon grains did not contain common Pb, implying no need for correction. Concordia ages and diagrams were obtained through reduction using IOLITE software (2.5 version-laboratory license). U-Pb diagrams were plotted using IsoplotR [55].

4. Morphology, Constituent Parts, and Petrography of the ca. 2.86 Ga Migmatites of the Carajás Domain

The migmatite morphology and its constituent parts are described using the definitions of Mehnert [56] and Sawyer [57], while the criteria of Holness [58], Holness and Sawyer [59], and Vernon [60] were applied in characterizing the migmatite textures.

4.1. Migmatite Morphologies

The Late Mesoarchean migmatites of the Carajás Domain occur as metatexites and diatexites in the Xingu Complex and the Xicrim-Cateté Orthogranulite. In these units, metatexite and diatexite migmatites display diffuse contacts with orthogneisses and granulites, which occur as the paleosome of these melt-bearing rocks. The metatexites within the Xicrim-Cateté Orthogranulite and Xingu Complex exhibit greater morphological variability than the diatexites. Metatexites have patch, stromatic, and net morphologies, which may coexist in the outcrops. Among these morphologies, stromatic are more common than net migmatites and patch migmatites.

The patch morphology is characterized by small (ca. 15–20 cm) and scattered spots of neosome in the paleosome. In the migmatites of the Xingu Complex, the patches contain hornblende porphyroblasts (peritectic phase) in a quartz–feldspar groundmass (Figure 2A), occurring in amphibolitic layers. The stromatic morphology encompasses parallel layers of leucosome surrounded by rims of hornblende or biotite (Figure 2B). The leucosome layers vary in thickness from ca. 1 to 15 cm and occur along the E-W foliation of the metamorphic rocks in the paleosome (Figure 2B). Figure 2C,D show the coexistence of stromatic and net morphologies, defining an array of parallel and intersecting leucosome layers. The leucosome layers in fractures, or boudin necks, shape the net structure (Figure 2C,D). The paleosome occurs as oriented fragments in the stromatic–net migmatite as shown in Figure 2C,D.

The diatexite migmatites show schollen and schlieren as the main morphologies. The schollen morphology is portrayed by dispersed, faceted, and angular fragments of the paleosome enclosed in an abundant hololeucocratic to leucocratic leucosome. The paleosome fragments are highly variable in size (ca. 1.5 to 5.0 m) and may or may not be oriented in the leucosome (Figure 2E). The schlieren morphology in diatexites consists of melanocratic stripes of residual hornblende or biotite (Figure 2E,F). The stripes are either continuous or discontinuous and predominantly narrow (up to 1 cm), with subordinated wider (up to 8 cm) occurrences (Figure 2F). Diatexites with schollen and schlieren morphologies may coexist in large outcrops (Figure 2E,F).

4.2. Constituent Parts of the Migmatites

4.2.1. Paleosome

The characterization of the paleosome follows the descriptive concept of Mehnert [56]. Therefore, the paleosome of the migmatites of the Xicrim-Cateté Orthogranulite encompasses (i) a mafic granulite and (ii) a diopside–enstatite orthogneiss. The contact between these lithotypes is complex and diffuse.

The mafic granulite is mainly equigranular and granoblastic but locally exhibits irregularly spaced compositional banding (Figure 3A). The rock is black, mesocratic, medium-grained (Figure 3A), and composed of plagioclase (~45 vol. %), enstatite (~15 vol. %), diopside (~12 vol. %), F–pargasite (~15 vol. %), biotite (~6 vol. %), quartz (3 vol. %), magnetite and ilmenite (3 vol. %), and zircon and apatite (~1 vol. %). It shows an interlobate fabric and elongated crystals of F–pargasite roughly defining its foliation (Figure 4A,B). It is also crosscut by white leucosomes (Figure 3A).

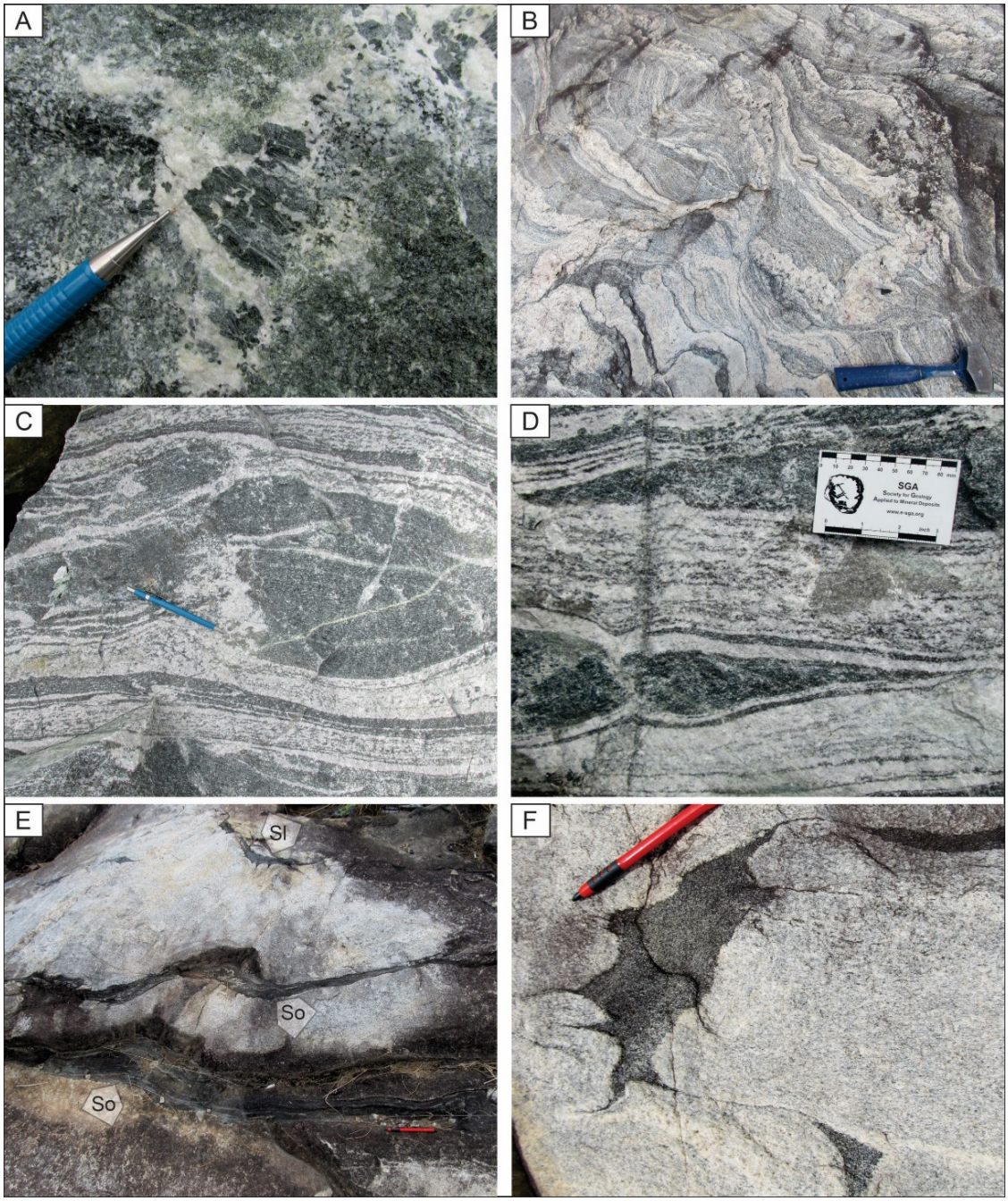

Figure 2. Migmatite morphologies: (**A**) patch morphology, characterized by spots of neosome with coarse-grained quartz, feldspar, and amphibole (site 2 in Figure 1); (**B**) stromatic morphology, defined by parallel layers of neosome within the paleosome. The neosome is segregated into thick leucosome parts (~5 cm) and narrow biotite-bearing melanosome rims (near site 5 in Figure 1); (**C**,**D**) stromatic and net morphology, exemplified by interconnected leucosome that surrounds angular to lensoidal fragments of the paleosome and occurs in boudin necks (site 2 in Figure 1); (**E**,**F**) large diatexite outcrop, where schollen (So; (**E**)) and schlieren (Sl; (**E**,**F**)) morphologies can be observed (site 5 in Figure 1).

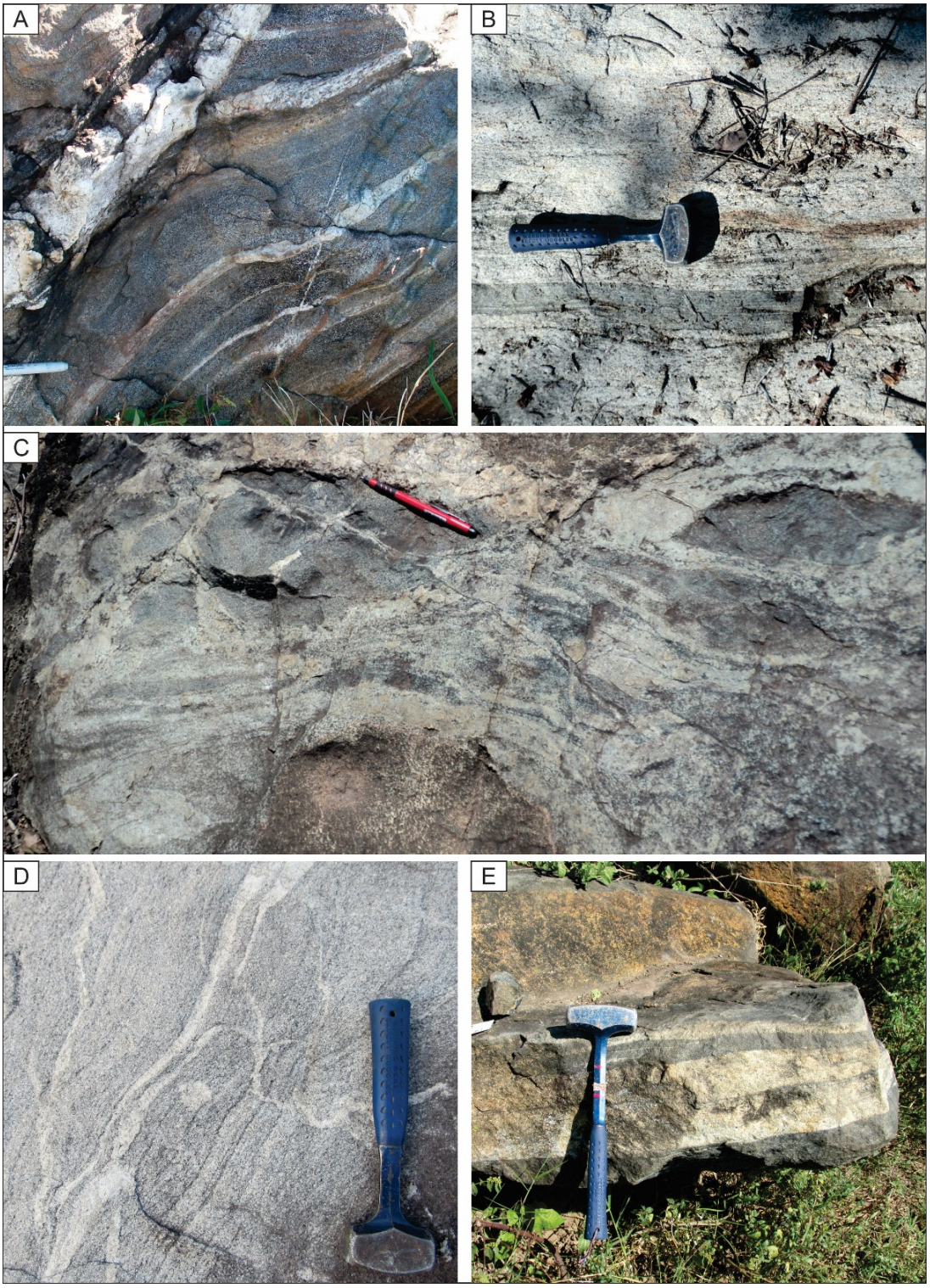

Figure 3. Paleosome of the migmatites from the Xicrim-Cateté Orthogranulite (**A**–**C**) and Xingu Complex (**D**,**E**). (**A**) Banded mafic granulite crosscut by discordant, white, coarse-grained leucosome (near site 3 in Figure 1); (**B**) image showing the compositional banding and gneissic foliation of the diopside–enstatite orthogneiss (near site 4 in Figure 1); (**C**) example of the complex geometric relationship between light-colored orthogneiss and dark mafic granulite in the diopside–enstatite orthogneiss (near site 3 in Figure 1); (**D**) illustration of the spaced foliation in the biotite orthogneiss (near site 5 in Figure 1); (**E**) image of the tabular compositional banding in the hornblende orthogneiss (site 7 in Figure 1).

The diopside–enstatite orthogneiss has thick bands (ca. 10–20 cm) of mafic granulite that locally define a compositional banding (Figure 3B). However, most of the rocks only exhibit a gneissic foliation. These structures show ENE-to-WNW strike and high (65–85°) dip angles to the south and north. The orthogneiss also hosts angular and amoeboid-shaped enclaves of mafic granulite (Figure 3C). The diopside–enstatite orthogneiss is gray, leucocratic, medium- to coarse-grained, and has an interlobate fabric (Figure 4C). It is composed of plagioclase (~50 vol. %), quartz (~20 vol. %), orthoclase (~5 vol. %), enstatite (~10 vol. %), diopside (~8 vol. %), hornblende and biotite (~6 vol. %), and magnetite, zircon, and apatite (~1 vol. %). Its foliation is defined by elongated enstatite, diopside, and biotite grains (Figure 4C). The rock shows several xenomorphic crystals of untwined K-feldspar in the corroded corners of quartz and K-feldspar (Figure 4D).

The paleosome of the Xingu Complex migmatites include (i) biotite orthogneiss with amphibolite lenses and (ii) hornblende orthogneiss with amphibolitic layers (Figure 3D,E). The biotite orthogneiss has ellipsoidal enclaves of amphibolite and spaced gneissic foliation (Figure 3D). It is gray, leucocratic, and medium-grained, displaying an interlobate fabric (Figure 4E). The biotite orthogneiss is composed of plagioclase (~45 vol. %), quartz (~20 vol. %), K-feldspar (orthoclase and microcline; ~20 vol. %), biotite (~12 vol. %), apatite (~2 vol. %), and minor amounts of magnetite, pistacite, clinozoisite, allanite, titanite, and zircon (~1 vol. %). Its ENE-to-WNW foliation with moderate to low dip angles to the north (25–45°) is defined by the alignment of biotite, plagioclase, and quartz ribbons (Figure 4E). The biotite orthogneiss contains several xenomorphic crystals of microcline and subordinated plagioclase in the corroded corners of quartz, plagioclase, and orthoclase crystals (Figure 4F).

The hornblende orthogneiss has thick (5 to 30 cm) melanocratic and hololeucocratic bands with ENE-to-WNW strike and low to moderate dip angles to the north (30–55°; Figure 3E). The contact between melanocratic and hololeucocratic layers is sharp (Figure 3E). The medium- to coarse-grained mesocratic to melanocratic layers are compositionally similar to amphibolite rocks and consist of hornblende (60–65 vol. %), plagioclase (30–35 vol. %), quartz (3–4 vol. %), titanite (~1 vol. %), apatite (~1 vol. %), rutile (~1 vol. %), epidote (~1 vol. %), zircon (~1 vol. %), magnetite (~1 vol. %), and pyrite (~1 vol. %).

The grain aggregate of the hornblende-bearing melanocratic layers shows a seriate interlobate fabric (Figure 4G), including poikiloblastic hornblende crystals with quartz, plagioclase, and apatite inclusions (Figure 4G). Xenomorphic cuspate crystals of quartz commonly occur in the boundaries of hornblende crystals.

The hololeucocratic layers are composed of coarse-grained idioblastic to subidioblastic plagioclase (~55 vol. %), quartz (~20–25 vol. %), orthoclase (~10 vol. %), hornblende (up to 10 vol. %), apatite (~1 vol. %), and zircon (~1 vol. %). The grain aggregate develops a seriate polygonal fabric (Figure 4H). The hololeucocratic layers with these compositional and textural characteristics only occur in orthogneisses that show no evidence (macroscopic or microscopic) of partial melting.

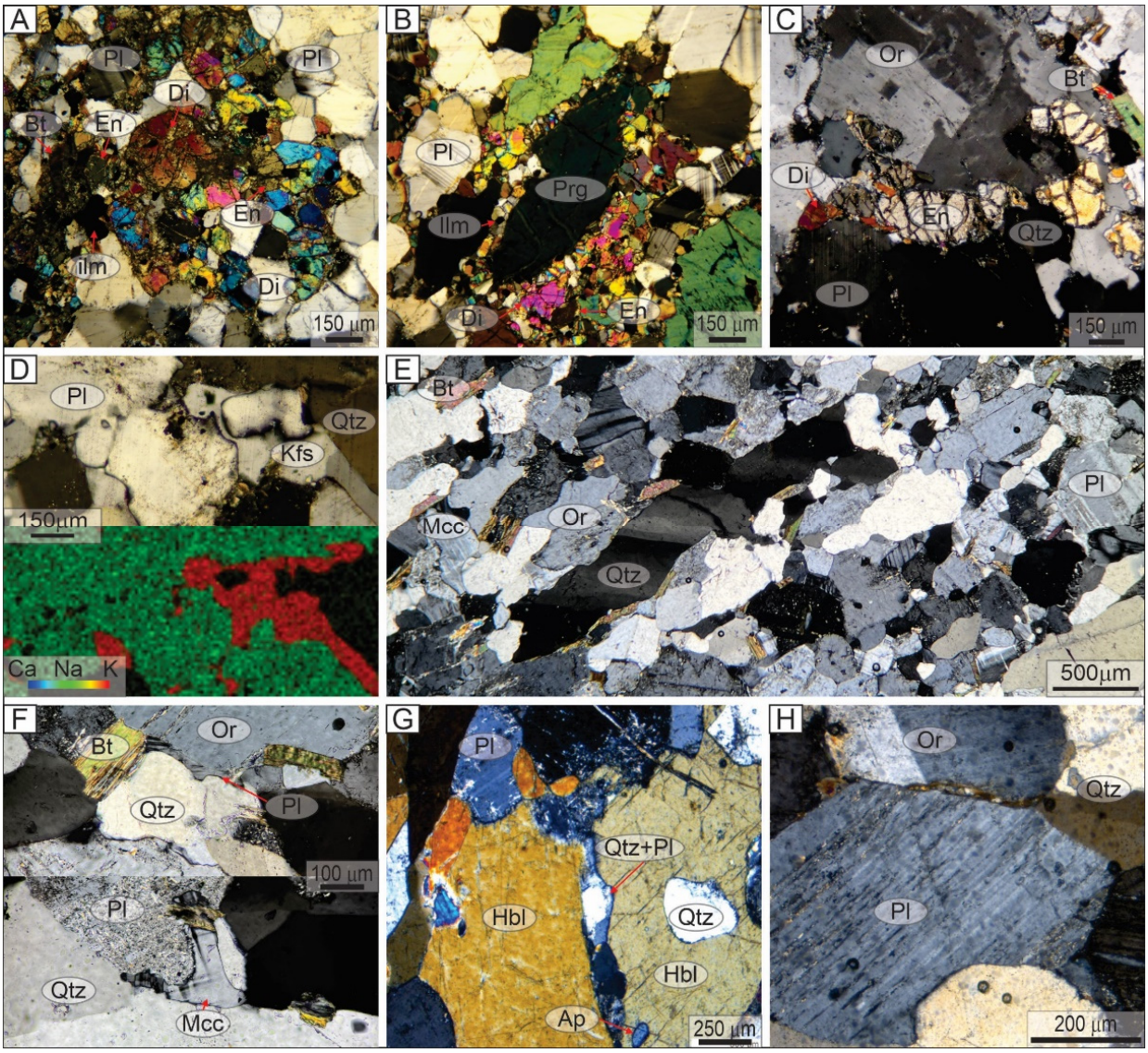

Figure 4. Photomicrographs of the paleosome of the migmatites from the Xicrim-Cateté Orthogranulite (**A**–**D**) and Xingu Complex (**E**–**H**). (**A**,**B**) The images show the polygonal fabric (**A**) and the rough foliation defined by pargasite crystals in the mafic granulite (**B**); (**C**) image of the interlobate fabric of the enstatite–diopside orthogneiss, illustrating the grain orientation that defines the gneissic foliation; (**D**) combination of a photomicrograph and energy-dispersive X-ray spectroscopy (EDS) ternary compositional map of Ca, Na, and K, showing the xenomorphic K-feldspar crystallized at the boundaries of quartz and plagioclase crystals in the enstatite–diopside orthogneiss; (**E**) illustration of the gneissic foliation defined by ribbon crystals of quartz, elongate crystals of plagioclase, biotite, and orthoclase in the biotite orthogneiss; (**F**) images of the xenomorphic crystals of plagioclase (upper) and microcline (lower), crystallized at the corners of orthoclase, plagioclase, and quartz crystals in the biotite orthogneiss; (**G**) example of the interlobate fabric of the dark band of the hornblende orthogneiss, with emphasis on the cuspate grains of quartz and plagioclase in the middle of hornblende crystals (the crystal on the right contains inclusions of apatite and quartz); (**H**) image of the polygonal fabric of the light band of the hornblende orthogneiss. Symbols for rock-forming minerals extracted from Warr [61]. Abbreviations: Ap (apatite); Bt (biotite); Di (diopside); En (enstatite); Ep (epidote); Hbl (hornblende); Kfs (K-feldspar); Mcc (microcline); Or (orthoclase); Pl (plagioclase); Prg (pargasite); Qtz (quartz). Photomicrographs are under cross-polarized transmitted light.

4.2.2. Neosome

The neosome in the migmatites of the Xicrim-Cateté Orthogranulite and Xingu Complex can be classified into four main types based on the relationship of its newly formed components: (i) unsegregated neosomes, (ii) white leucosomes, (iii) pink leucosomes, and (iv) hornblende- or biotite-bearing melanosomes. The unsegregated neosome is leucocratic and encloses the scattered spots with coarse-grained quartz, plagioclase, K-feldspar, and hornblende that define the morphology of patch migmatites of the Xingu Complex (see Figure 2A).

In the metatexite migmatites of the Xicrim-Cateté Orthogranulite, the white leucosome (Figure 5A) is composed of plagioclase (~43 vol. %), quartz (~27 vol. %), orthoclase (~26 vol. %), biotite (~1 vol. %), magnetite (~1 vol. %), apatite (~1 vol. %), and zircon (~1 vol. %). The leucosome is hololeucocratic, coarse-grained, and porphyritic (Figure 5A). The porphyritic texture is characterized by idiomorphic to subidiomorphic crystals of plagioclase (up to 2 cm) in a groundmass of idiomorphic to subidiomorphic coarse-grained orthoclase and quartz (Figure 6A).

The minor phases occur as scattered fine-grained grains or as inclusions in the phenocrysts. The leucosome also contains local micrographic intergrowths of xenomorphic quartz and orthoclase in the groundmass (Figure 6A).

In the metatexite and diatexite migmatites of the Xingu Complex, the white leucosome occurs in segregated neosome patches surrounded by coronas of coarse hornblende (Figure 5B), in leucosome layers (metatexites; Figure 5C), or as pervasive leucocratic masses (diatexites; see Figure 2E,F). The leucosome is composed of plagioclase (~45 vol. %), quartz (~30 vol. %), microcline (~20 vol. %), hornblende (1 vol. %), biotite (1 vol. %), apatite (1 vol. %), ilmenite and magnetite (1 vol. %), and zircon, epidote, allanite, and chamosite (1 vol. %). It is hololeucocratic and coarse-grained, showing a seriate grain size distribution (Figure 6B). The texture of the leucosome consists of idiomorphic plagioclase and subidiomorphic quartz grains surrounded by xenomorphic crystals of microcline, with minor phases dispersed in the groundmass (Figure 6B). Phenocrysts of quartz locally exhibit plastic deformation features, such as chessboard extinction and core-and-mantle textures (Figure 6C).

The pink leucosome of migmatites of the Xingu Complex (Figure 5D) was found exclusively in the diatexite migmatites of the northeastern portion of the Xingu Complex (site 1 in Figure 1). It is composed of quartz (~30 vol. %), plagioclase (~30 vol. %), microcline (~35 vol. %), and chlorite (~10 vol. %; Figure 4F). The leucosome is leucocratic, coarse-grained, and inequigranular (Figure 5D). Its porphyritic texture is characterized by xenomorphic microcline phenocrysts in a groundmass of idiomorphic to subidiomorphic plagioclase and quartz crystals (Figure 6D). The microcline crystals also enclose intergrown plagioclase and quartz crystals (Figure 6D). The idiomorphic chlorite crystals are dispersed in the groundmass.

The biotite-bearing melanosome that surrounds the leucosome in the migmatites of the Xicrim-Cateté Orthogranulite (Figure 5E) consists of untwined plagioclase (~45 vol. %), reddish-brown biotite (~40 vol. %), quartz (~5 vol. %), magnetite (~5 vol. %), relicts of enstatite and diopside (~4 vol. %), and epidote (~1 vol. %). It is medium-grained and inequigranular, exhibiting a polygonal to interlobate fabric (Figure 6E). The melanosome contains interstitial idioblastic to subidioblastic crystals of biotite, magnetite, and xenomorphic crystals of quartz that crystallized along the corroded boundaries of plagioclase grains (Figure 6E). These phases also replace enstatite and diopside (Figure 6E). Additionally, the xenomorphic quartz locally includes biotite near the pyroxene boundaries (Figure 6E). Biotite was subsequently replaced by idioblastic epidote crystals (Figure 6E).

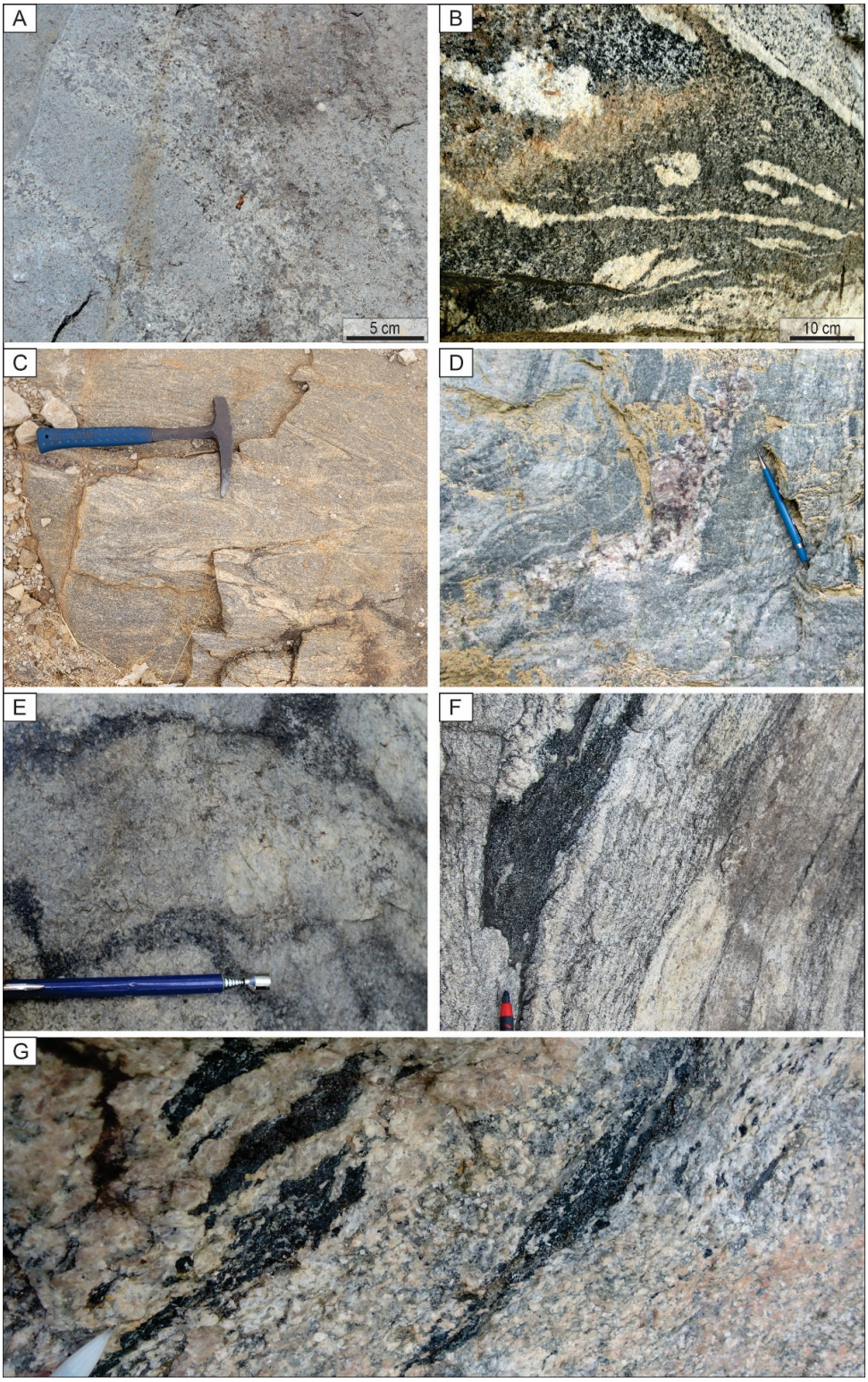

Figure 5. Neosome of the migmatites from the Xicrim-Cateté Orthogranulite (**A**,**E**) and Xingu Complex (**B**–**D**,**F**,**G**). (**A**) Example of the coarse-grained leucosome in the gray diopside–enstatite orthogneiss of the Xicrim-Cateté Orthogranulite (site 6 in Figure 1); (**B**,**C**) illustration of the white leucosome in the hornblende (**B**) and biotite (**C**) orthogneiss of the Xingu Complex (sites 2 and 8, respectively, in Figure 1); (**D**) image of the coarse-grained pink leucosome injected into a schollen diatexite (site 1 in Figure 1); (**E**) detail of the biotite-bearing melanosome surrounding the white leucosome in neosome layers of the diopside–enstatite orthogneiss (site 4 in Figure 1); (**F**) view of the biotite-bearing melanosome observed in a stromatic metatexite (near site 5 in Figure 1); (**G**) image of the hornblende-bearing melanosome detected in the schlieren diatexite (near site 5 in Figure 1).

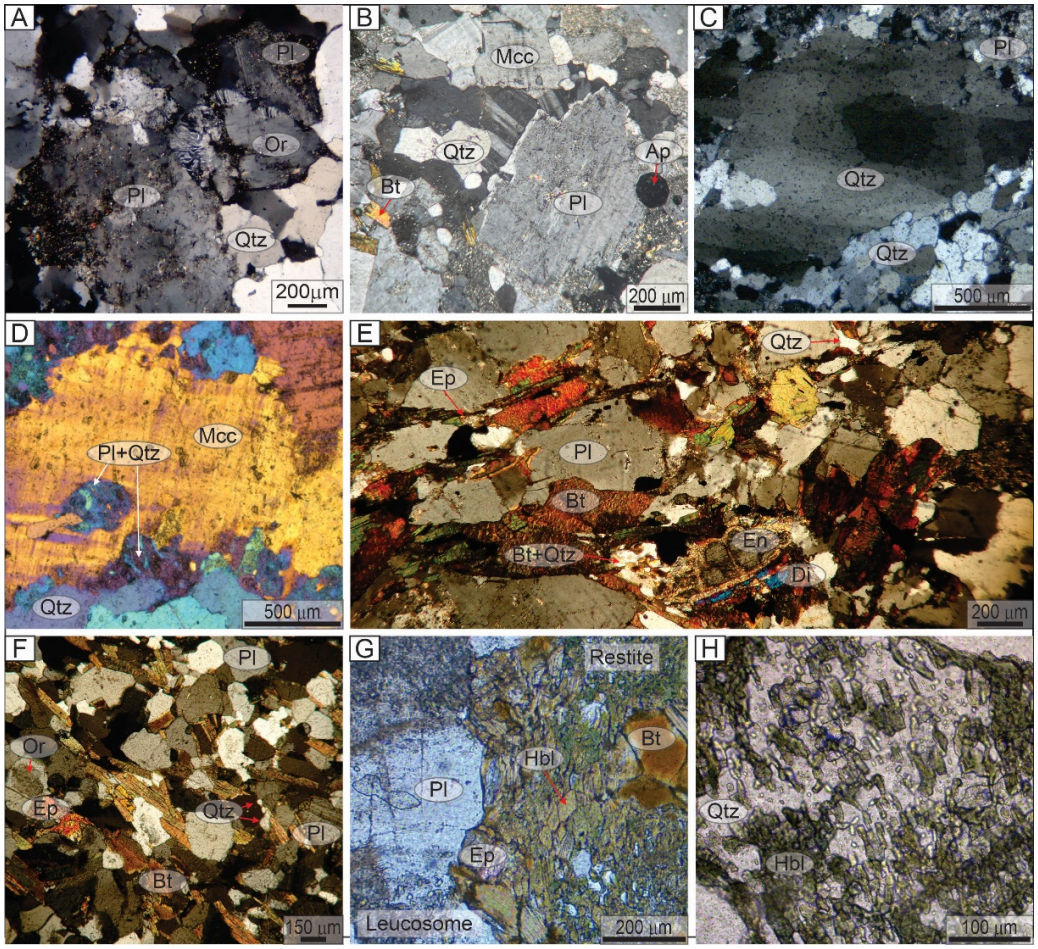

Figure 6. Photomicrographs of the neosome of the migmatites from the Xicrim-Cateté Orthogranulite (**A**,**E**) and Xingu Complex (**B**–**D**,**F**–**H**). (**A**) Detail of the leucosome layer (Figure 4E) of the diopside–enstatite orthogneiss, showing plagioclase phenocrysts and a micrographic texture; (**B**,**C**) images of the leucosome layers showing idiomorphic crystals of plagioclase and microcline (**B**), and deformation features of large quartz crystals (**C**) of the white leucosome; (**D**) example of xenomorphic microcline crystals in the pink leucosome; (**E**) illustration of the biotite-bearing melanosome in the neosome layer shown in Figure 4E, revealing interstitial quartz, biotite, and magnetite in the corners of plagioclase, as well as intergrowths of biotite and quartz at the boundaries of enstatite; (**F**) picture of the equigranular biotite-bearing melanosome in the migmatites of the Xingu Complex; (**G**,**H**) images of the hornblende-bearing melanosome showing idiomorphic crystals of hornblende being replaced by biotite (**G**), and the symplectitic texture developed between hornblende and quartz (**H**). Symbols for rock-forming minerals extracted from Warr [61]. Abbreviations: Ap (apatite); Bt (biotite); Di (diopside); En (enstatite); Ep (epidote); Hbl (hornblende); Kfs (K-feldspar); Mcc (microcline); Or (orthoclase); Pl (plagioclase); Qtz (quartz). Photomicrographs were taken under cross-polarized light. One-wave quartz plate was used for photomicrograph D.

The biotite-bearing melanosome observed in the migmatites of the Xingu Complex (Figure 5G) is composed of plagioclase (~45 vol. %), brown biotite (~40 vol. %), quartz (~9 vol. %), orthoclase (~3 vol. %), and epidote (~3 vol. %). It is medium-grained, displaying a polygonal fabric and an equigranular grain size distribution (Figure 6F). The melanosome contains xenomorphic crystals of quartz, which are often found between the idioblastic plagioclase and biotite (Figure 6F). Late idioblastic epidote crystals replace biotite in the melanosome (Figure 6F).

The hornblende-bearing (Figure 5F) melanosome of migmatites of the Xingu Complex is composed of fine-grained quartz (~3 vol. %) and plagioclase (~10 vol. %), medium- to coarse-grained idioblastic to subidioblastic hornblende crystals (~80 vol. %), biotite

(~3 vol. %), magnetite (~1 vol. %), and fine-grained hastingsite (~2 vol. %) and epidote (~1 vol. %). The melanosome exhibits an interlobate to polygonal fabric with a seriate grain size distribution (Figure 6G). Toward the contact between the melanosome and leucosome, hornblende crystals increase in size and are extensively replaced by idioblastic biotite (Figure 6G). Also, locally, hornblende and quartz crystals develop a symplectitic texture (Figure 6H). Late epidote and hastingsite also replaced hornblende crystals in the melanosome.

5. Mesoarchean Syntectonic Granitoids

The ca. 2.92–2.83 Ga syntectonic granitoids were extensively mapped, described, chemically and isotopically characterized, and dated over decades of research in the Carajás Province (e.g., [13–15,17,18]). The following description focuses on the characterization of the newly identified Mesoarchean hercynite metadiorite and the contact relationships between syntectonic granitoids and other units at sites unaffected by later deformational events.

Two contact types among hercynite metadiorite, syntectonic granitoids, migmatites, and orthogneisses stand out: (i) sharp and (ii) interdigitated diffuse. Examples of situation (i) were observed in the northeastern and central portions of the Carajás Domain (site 1 and near site 5 in Figure 1). At site 1, the hercynite metadiorite forms a sharp contact with diatexites of the Xingu Complex, which dominate the walls of the Britamil quarry (Figure 7A), and is crosscut by pink leucosome injections (Section 4.2.2; Figure 7A). The metadiorite is composed of plagioclase (~65 vol. %), hornblende (~20 vol. %), K-feldspar (~4 vol. %), dark green hercynite (~5 vol. %), and quartz (~3 vol. %), showing a subordinated content (~3 vol. %) of chlorite, apatite, chlorapatite, epidote, zircon, titanite, ilmenite, rutile, magnetite, chalcopyrite, pyrite, and allanite (Figure 8A). At site 5, a syntectonic porphyritic granodiorite of the Água Limpa Suite ([18]) occurs as sheets of variable thickness (1 to 2 m) within the gneissic foliation of a biotite orthogneiss of the Xingu Complex (Figure 7B). The plagioclase phenocrysts in the granodioritic rock are mostly oriented but not extensively recrystallized, preserving their idiomorphic shape (Figure 7B).

An example of the situation (ii) was observed near sites 5 and 6 in Figure 1, in the central portion of the Carajás Domain (Figure 7C). At these sites, fragments of Xingu biotite orthogneiss and biotite-rich stripes gradually disappear into a biotite granite of the Nova Canadá Granodiorite [16]. The granitoid exhibits deformed boundaries and an isotropic core (Figure 7D,E). The foliated boundaries show ENE-to-WNW strike and moderate dip angles to the north and south (~50°).

The composition of the biotite granite of the Nova Canadá Granodiorite is similar to the white leucosomes of the Xingu Complex migmatites, consisting of quartz (~25 vol. %), plagioclase (~25 vol. %), orthoclase (~20 vol. %), microcline (~15 vol. %), biotite (~5 vol. %), and small amounts (~5 vol. %) of epidote, apatite, zircon, and magnetite. The rock is hololeucocratic, beige, and inequigranular (Figure 7D,E). Plagioclase, orthoclase, and microcline form idiomorphic to subidiomorphic megacrysts, which characterize the porphyritic texture in a medium-grained groundmass of biotite granite (Figure 8B,C). Toward the foliated boundary of the granitoid, the minerals initially develop an orientation but mostly preserve their shapes (Figure 8D). Progressively, the rock develops an interlobate fabric that contains (i) biotite crystals clustered into sinuous foliations; (ii) fine-grained quartz subgrains with undulose extinction; (iii) bent and fractured crystals of plagioclase, orthoclase, and microcline with marginal subgrains (Figure 8E).

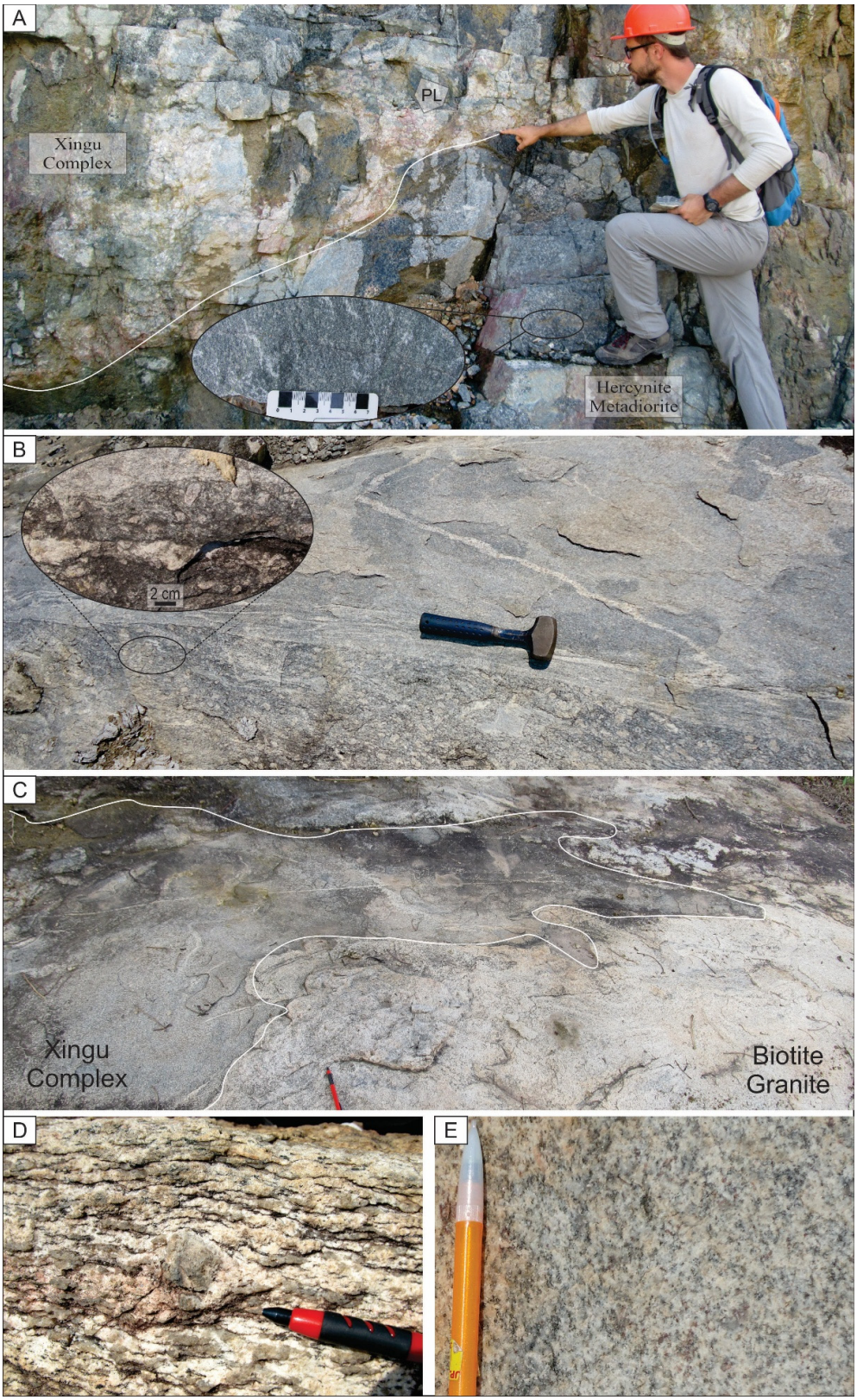

Figure 7. Syntectonic granitoids. (**A**) Image showing the sharp contact between hercynite metadiorite and the Xingu Complex. The metadiorite is crosscut by pink leucosome injections; (**B**) illustration of the sharp intrusive contact between sheets of blasto-porphyritic metagranodiorite and gray orthogneiss of the Xingu Complex. The zoomed-in image highlights the oriented idiomorphic crystals of K-feldspar; (**C**) diffuse contact between orthogneiss of Xingu Complex and biotite granite (Schollen Diatexite); (**D**,**E**) biotite porphyritic granite pluton with foliated boundaries (**D**) and an isotropic core (**E**).

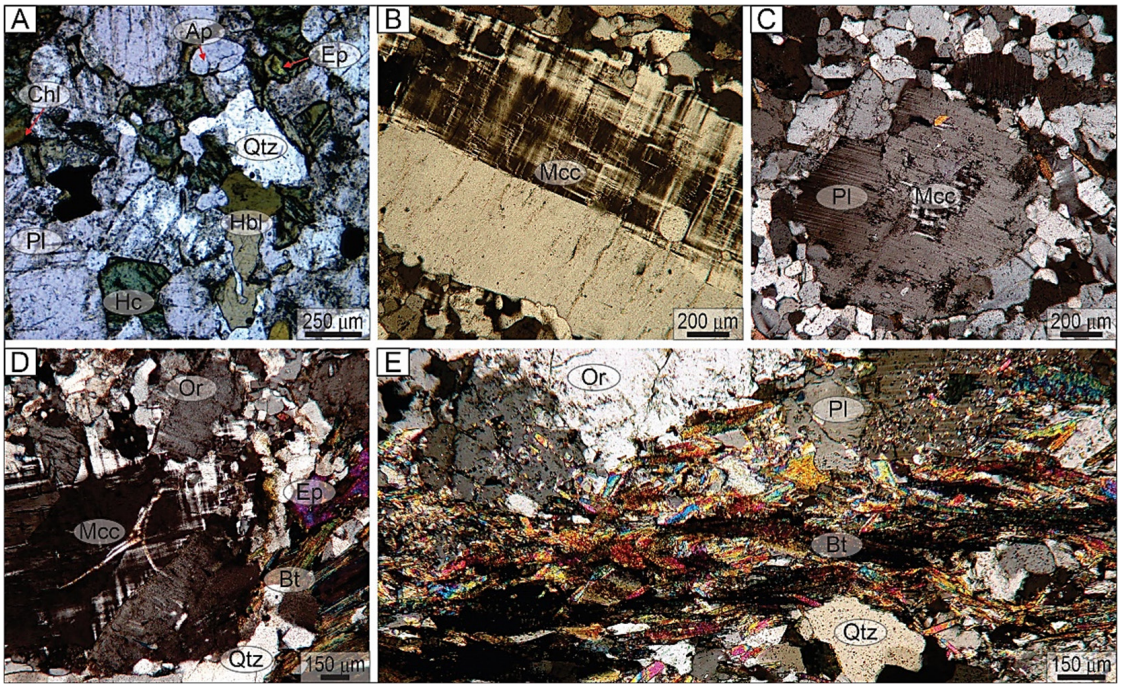

Figure 8. Microstructure of the hercynite metadiorite (**A**) and biotite granite (**B**–**E**). (**A**) The image highlights relics of idiomorphic to subidiomorphic plagioclase crystals, surrounded by xenomorphic to subidiomorphic hercynite and hornblende. (**B**,**C**) Images illustrating the phenocrysts of orthoclase (**A**), microcline (**B**), and plagioclase (**C**), which define the porphyritic texture of the biotite granite; (**D**) the picture displays the alignment of idiomorphic grains of orthoclase, biotite, and epidote, as well as the occurrence of interstitial microcline near the boundary of the biotite granite; (**E**) the image emphasizes the sinuous foliation developed by subidioblastic biotite grains at the granitoid boundary, along with the folded and fractured plagioclase in the upper right and the lobate boundaries between two orthoclase crystals in the upper left. Symbols for rock-forming minerals extracted from Warr [61]. Abbreviations: Ap (apatite); Bt (biotite); Chl (chlorite); Ep (epidote); Hbl (hornblende); Hc (hercynite); Mcc (microcline); Or (orthoclase); Pl (plagioclase); Qtz (quartz). Photomicrographs taken under transmitted and cross-polarized light.

6. Geochemical Characteristics of the Leucosome in the Migmatites of the Xicrim-Cateté Orthogranulite and Xingu Complex

The leucosome samples were collected from metatexites and diatexites of the Xicrim-Cateté Orthogranulite (SM36L1, SM36L2, SM41L, SM39N; see numbers 3 and 4 in Figure 1; Table 1) and the Xingu Complex (1G1, 1G2, 1G3, 1G4, 1G5, 1G6, 1G7, XS24L, XS37L, 1J1, 1J2, 1J3; see numbers 1, 5, and 6 in Figure 1; Table 1). Additionally, the lithochemical data of these leucosome samples were plotted alongside compiled data from the crustal-derived, calc-alkaline to alkaline group of syntectonic granitoids (n: 44; [13–15,17]). The dataset of syntectonic granitoids is available in Supplementary Table S1. The diagrams in this study will support further discussions on the relationship between the leucosomes and granitoids.

Table 1. Lithochemical data of leucosomes of the Xicrim-Cateté Orthogranulite and Xingu Complex. Eu/Eu* ratios were calculated by the formula $Eu/\sqrt{Sm \cdot Gd}$, using values normalized by the C1 chondrite [62].

Rock Type	**White Leucosome: Xicrim-Cateté Orthogranulite**				**White Leucosome: Xingu Complex**									**Pink Leucosome: Xingu Complex**		
Sample	**SM36L1**	**SM36L2**	**SM41L**	**SM39N**	**1G1**	**1G2**	**1G3**	**1G4**	**1G5**	**1G6**	**1G7**	**XS24L**	**XS37L**	**1J1**	**1J2**	**1J3**
Oxides (wt%)																
SiO_2	69.90	70.04	72.86	63.38	71.45	72.21	71.42	72.03	70.64	71.71	72.46	77.10	74.80	75.90	73.85	72.79
TiO_2	0.21	0.19	0.04	0.50	0.18	0.11	0.18	0.19	0.22	0.16	0.17	0.07	0.10	0.06	0.07	0.04
Al_2O_3	16.80	16.55	15.88	16.58	15.50	15.09	15.44	15.35	15.67	15.32	15.09	13.50	13.65	12.69	14.27	14.54
FeO_t	1.97	1.65	0.67	4.56	1.42	0.93	1.34	1.32	1.50	1.15	1.12	0.96	1.28	0.29	0.68	0.49
MnO	0.02	0.03	0.01	0.06	0.02	0.02	0.03	0.02	0.02	0.02	0.02	0.01	0.01	0.01	0.01	0.01
MgO	0.65	0.87	0.24	2.12	0.48	0.28	0.47	0.45	0.52	0.46	0.39	0.18	0.24	0.18	0.11	0.05
CaO	3.74	4.29	3.14	4.65	2.21	1.71	1.86	2.07	2.38	1.66	1.87	1.46	1.15	0.60	1.03	0.55
Na_2O	4.90	4.51	4.63	4.98	5.13	4.71	5.38	5.20	5.14	5.26	4.93	4.19	2.65	2.62	3.84	3.19
K_2O	1.45	0.84	1.75	1.41	2.50	3.66	2.46	2.55	2.38	2.96	2.90	2.88	5.74	6.38	5.23	7.49
P_2O_5	0.11	0.04	0.03	0.14	0.07	0.05	0.07	0.07	0.08	0.06	0.07	0.02	0.03	0.02	0.09	0.02
LOI	0.58	0.60	0.40	0.90	0.67	0.55	0.67	0.69	0.73	0.72	0.57	0.22	0.31	0.50	0.41	0.39
Total	100.74	99.84	99.75	99.77	99.80	99.40	99.50	100.10	99.50	99.60	99.70	101.08	100.41	99.30	99.70	99.60
Trace elements (ppm)																
Zr	75.0	34.3	67.3	118.8	115.4	82.1	98.7	93.7	106.7	93.9	97.3	62.0	176.0	33.8	51.8	74.6
Zn	34.0	11.0	9.0	46.0	28.5	22.1	28.6	27.0	26.0	24.7	23.2	26.0	23.0	18.1	13.6	10.4
Rb	30.9	7.7	24.1	30.5	56.4	82.6	52.3	37.4	22.9	73.3	31.0	47.3	104.5	122.0	95.4	144.0
Sr	731	615	564	625	414	372	255	225	186	354	227	663	308	198	223	129
Y	2.00	2.20	1.20	10.90	2.52	2.13	2.36	2.15	2.26	1.86	1.62	1.00	2.80	0.93	3.28	0.70
Nb	2.00	1.40	0.40	3.80	2.71	1.64	2.28	2.34	4.08	1.59	1.80	1.00	2.20	2.48	1.08	0.54
Ta	0.10	n.d	n.d	0.10	0.06	0.06	0.14	0.08	0.07	0.07	0.14	0.10	0.30	0.25	0.09	0.08
Ba	1010	529	1432	548	744	961	698	691	855	747	1032	2620	2360	1954	1469	1435
La	27.80	13.50	15.20	26.60	14.75	11.25	10.73	10.13	9.21	13.23	9.65	6.90	60.70	10.41	12.81	4.05
Ce	45.20	20.10	21.20	48.20	25.05	19.09	24.73	15.42	11.57	22.44	14.92	11.10	111.50	12.67	20.81	2.87
Pr	4.27	1.91	1.78	5.81	2.57	2.06	1.86	1.92	1.56	2.43	1.89	1.20	10.65	1.73	2.66	0.58
Nd	13.00	6.20	5.20	22.30	8.36	6.75	6.26	6.40	5.18	7.91	6.45	4.00	32.30	5.21	9.00	1.82
Sm	1.72	0.74	0.49	3.96	1.38	1.14	1.10	1.10	0.91	1.38	1.05	0.55	3.69	0.75	1.71	0.33
Eu	0.73	0.64	0.60	1.00	0.68	0.55	0.45	0.46	0.62	0.52	0.52	0.28	0.53	0.68	0.64	0.55
Gd	0.82	0.59	0.37	3.31	1.14	0.89	0.93	0.86	0.79	0.98	0.78	0.42	1.32	0.54	1.32	0.26
Tb	0.07	0.07	0.03	0.39	0.12	0.10	0.09	0.09	0.09	0.10	0.08	0.02	0.17	0.05	0.16	0.03
Dy	0.43	0.32	0.21	2.08	0.56	0.43	0.43	0.45	0.48	0.38	0.31	0.13	0.65	0.20	0.77	0.15
Ho	0.07	0.07	0.03	0.37	0.09	0.08	0.07	0.07	0.08	0.07	0.06	0.02	0.11	0.04	0.13	0.03
Er	0.18	0.26	0.09	1.03	0.25	0.20	0.21	0.20	0.20	0.18	0.17	0.06	0.29	0.11	0.34	0.09
Tm	0.04	0.03	0.02	0.14	0.03	0.03	0.03	0.02	0.02	0.02	0.02	0.02	0.06	0.01	0.04	0.01
Yb	0.18	0.13	0.16	0.92	0.17	0.17	0.16	0.15	0.14	0.14	0.14	0.14	0.31	0.09	0.26	0.11
Lu	0.02	0.03	0.01	0.12	0.03	0.03	0.03	0.03	0.03	0.03	0.02	0.02	0.04	0.02	0.04	0.02
Hf	1.90	0.70	2.30	3.10	3.25	2.59	2.82	2.72	3.03	2.79	2.94	2.00	5.20	1.16	1.74	4.37
Pb	11.00	0.90	1.20	4.10	11.33	14.71	8.57	11.40	9.84	11.25	10.06	20.00	17.00	14.65	9.53	14.44

Table 1. *Cont.*

Rock Type	White Leucosome: Xicrim-Cateté Orthogranulite				White Leucosome: Xingu Complex									Pink Leucosome: Xingu Complex		
Sample	**SM36L1**	**SM36L2**	**SM41L**	**SM39N**	**1G1**	**1G2**	**1G3**	**1G4**	**1G5**	**1G6**	**1G7**	**XS24L**	**XS37L**	**1J1**	**1J2**	**1J3**
Th	2.15	0.30	0.40	1.30	1.65	2.10	4.04	2.33	0.55	3.33	2.13	2.19	18.80	3.75	3.74	2.28
U	n.d	n.d	0.20	n.d	0.37	0.78	1.06	0.50	0.40	0.83	0.64	0.94	1.29	1.27	0.45	3.18
Oxide and trace element ratios																
Na_2O/K_2O	3.38	5.37	2.65	3.53	2.05	1.29	2.19	2.04	2.16	1.78	1.70	1.45	0.46	0.41	0.73	0.43
ASI	1.02	1.03	1.04	0.91	1.02	1.02	1.04	1.02	1.02	1.03	1.03	1.07	1.08	1.03	1.03	1.01
Fe-index	0.75	0.65	0.74	0.68	0.75	0.77	0.74	0.75	0.74	0.71	0.74	0.84	0.84	0.62	0.86	0.91
MALI	2.61	1.06	3.24	1.74	5.42	6.66	5.98	5.68	5.14	6.56	5.96	5.61	7.24	8.4	8.04	10.13
La_N/Yb_N	104.92	70.55	64.54	19.64	58.94	44.96	45.56	45.88	44.69	64.20	46.82	33.48	133.02	78.58	33.47	25.01
Eu/Eu*	1.87	2.95	4.30	0.84	1.65	1.66	1.36	1.44	2.23	1.36	1.75	1.78	0.73	3.26	1.30	5.72
Sr/Y	366	279	470	57	164	174	108	105	82	190	140	663	110	213	68	185
Normative feldspar proportions																
Or	8.57	4.96	10.34	8.33	14.77	21.63	14.54	15.07	14.07	17.49	17.14	17.02	33.92	37.70	30.91	44.26
Ab	41.46	38.16	39.18	42.14	43.41	39.86	45.52	44.00	43.49	44.51	41.72	35.46	22.42	22.17	32.49	26.99
An	17.84	21.02	15.38	18.72	10.51	8.16	8.77	9.81	11.29	7.84	8.82	7.11	5.51	2.85	4.52	2.60

6.1. Major, Minor, and Trace Element Compositions

The white and pink leucosome samples show SiO_2 concentrations varying from 63.38 to 77.10 wt%, with acid rock types dominating over intermediate ones (sample SM39N; Table 1). Al_2O_3 concentrations vary from 12.69 to 16.80 wt%, showing a negative correlation with SiO_2 (Table 1). The normative proportions of albite (22.17% to 45.52%), anorthite (2.60% to 21.02%), and orthoclase (4.96% to 44.26%) define a compositional spectrum in which white leucosomes exhibit tonalitic, trondhjemitic, and granitic composition, while pink leucosomes have a granitic composition (Table 1; Figure 9A).

The anorthite proportion correlates with the Na_2O/K_2O ratio, which varies from 5.37 to 0.41, and defines a continuous trend between sodic (white) and potassic (white and pink) leucosome samples (Table 1). Such a tendency also appears in the cationic Ca–Na–K diagram, where the white and pink leucosomes occupy an intermediate position between the TTG field and the calc-alkaline trend (Figure 9B). The diagram also shows that the samples do not follow the trondhjemitic trend (Figure 9B).

The modified alkali–lime index (MALI) classifies the white leucosomes as predominantly calc-alkalic, with some subordinate calcic types, and the pink leucosomes as alkalic-calcic and alkalic types (Figure 9C). The calcic and calc-alkaline white leucosomes are also magnesian, apart from two MgO-poor samples ($XS24L_{MgO}$: 0.18 wt%; $XS37L_{MgO}$: 0.24 wt%), which show a ferroan tendency (Figure 9D). Among the alkalic-calcic and alkalic pink leucosomes, only the FeOt-poor (0.29 wt%) sample 1J1 plots in the magnesian field (Figure 9D). The samples of white and pink leucosomes plot in the peraluminous field of the alumina saturation index (ASI) diagram, except for the calcic and magnesian sample SM39N, which shows a metaluminous character (ASI: 0,91; Table 1; Figure 9E).

The rare earth element (REE) multi-element diagram (Figure 9F) reveals a fractionated pattern between light REE (LREE) and heavy REE (HREE) in the leucosome samples, with $(La/Yb)_N$ ratios varying from 19.6 to 133 (Table 1). The diagram also portrays the variability of the Eu/Eu* ratio (Figure 9F), which ranges from 0.73 to 5.72 (Table 1). Only two samples (XS37L and SM39N) show negative Eu anomalies, with Eu/Eu* ratios of 0.73 and 0.84 (Table 1).

The diagrams of Figure 8 also show that the compiled samples of syntectonic granitoids and white and pink leucosomes share similar compositions. In Figure 9A, granitoid and leucosome samples define parallel evolving trends from tonalites to granites. Figure 9B shows a K enrichment of the whole dataset between the TTG field and the calc-alkaline trend. Figure 9C–E reveal that most of the granitoids are calc-alkalic, magnesian, and peraluminous, similar to the majority of the leucosome samples. In addition, the subordinated compositions among the granitoids are also matched by the leucosome samples (Figure 9C–E). The multi-element REE diagram also reveals that the fractionated pattern observed in the leucosome samples occurs among the granitoids (Figure 9F).

6.2. Binary Vector Diagrams

The binary diagrams in Figure 10 were produced to highlight differences between the leucosome and granitoid datasets. These figures show their separation into clusters that intersect with each other. The relationship between these data clusters and mineral vectors is described below.

The La vs. Yb diagram reveals that the white and pink leucosome have lower contents of La and Yb than the granitoid samples (Figure 10A). This compositional variation defines a trend that aligns with the biotite, K-feldspar, and plagioclase vectors (Figure 10A). The Rb vs. Yb diagram emphasizes the complementary enrichment of Rb in the granitoids, which also defines a trend line between the clusters (Figure 10B). In this case, the alignment of the datasets is parallel to the plagioclase vector (Figure 10B).

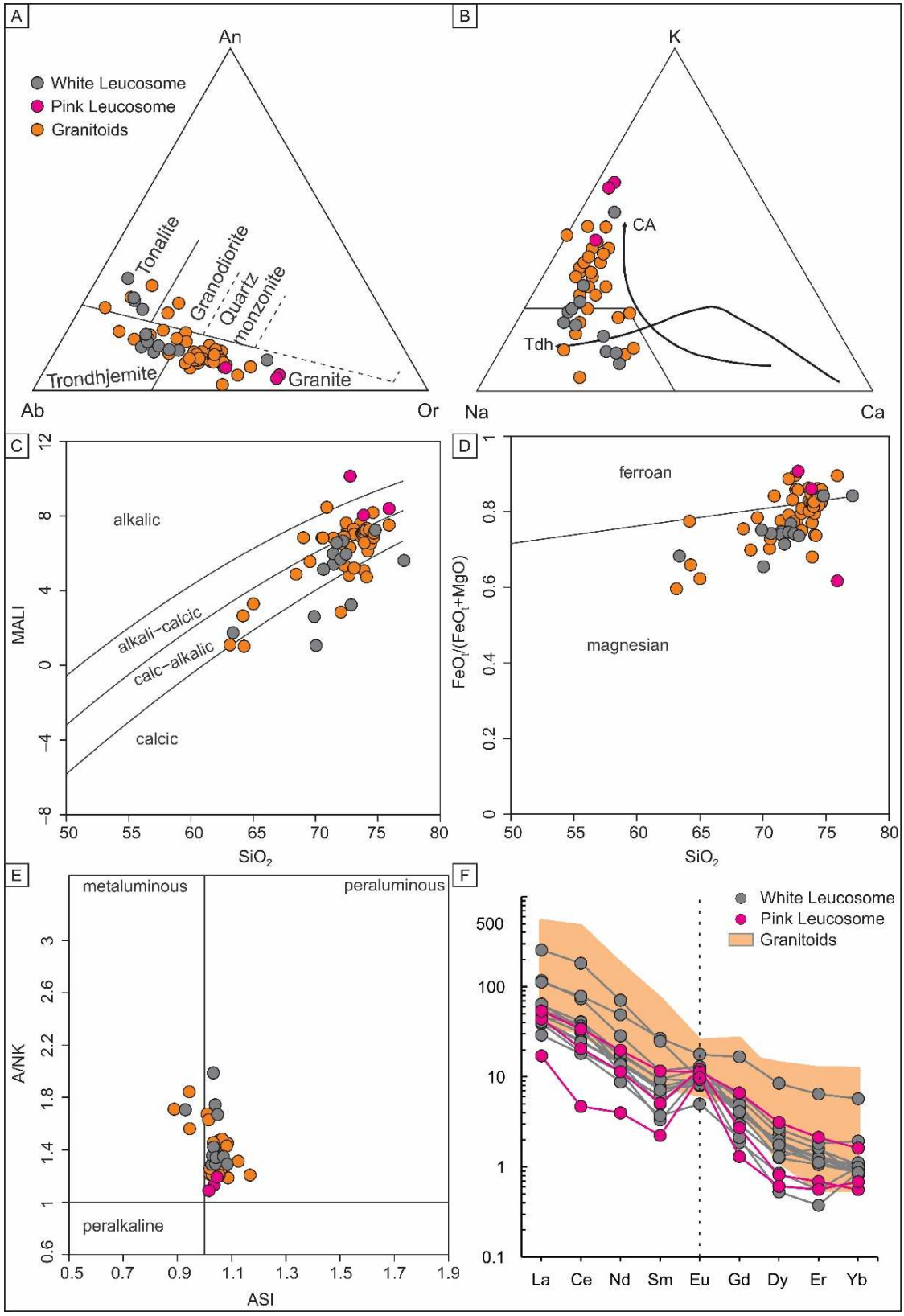

Figure 9. (**A**–**E**) Granite classification diagrams for white and pink leucosomes and the compiled samples of syntectonic granites. (**A**) Feldspar triangle of O'Connor [63]; (**B**) K-Na-Ca ternary plot with calc-alkaline (CA) and trondhjemitic evolution lines; (**C**) SiO_2 vs. modified alkali–lime index [64]; (**D**) SiO_2 vs. Fe-index [64]; (**E**) aluminum saturation index diagram based on Shand [65]; (**F**) multi-elementary rare earth element plot.

The Eu/Eu* vs. Yb plot demonstrates that the white and pink leucosome and granitoid datasets can be separated in terms of Eu anomaly, which is mostly positive for the leucosome samples and mostly negative for the granitoid samples (Figure 10C). However, the datasets intersect around Eu/Eu* = 1 (Figure 10C). The plagioclase vector runs parallel to the enrichment of Yb and the decrease in Eu/Eu* ratios (Figure 10C).

The white and pink leucosome and granitoids datasets overlap more in the Sr/Y vs. Y diagram (Figure 10D). The separation into distinct clusters is not as straightforward as observed in Figure 10A–C. Only three leucosome samples (SM36L1, SM41L, XS24L) completely detach from the granitoid dataset, forming an independent group (Figure 10D). As observed in Figure 10B,C, the Sr/Y vs. Y plot shows a trend of Y enrichment and Sr depletion from leucosome to granitoids, which is also parallel to the plagioclase vector (Figure 10D).

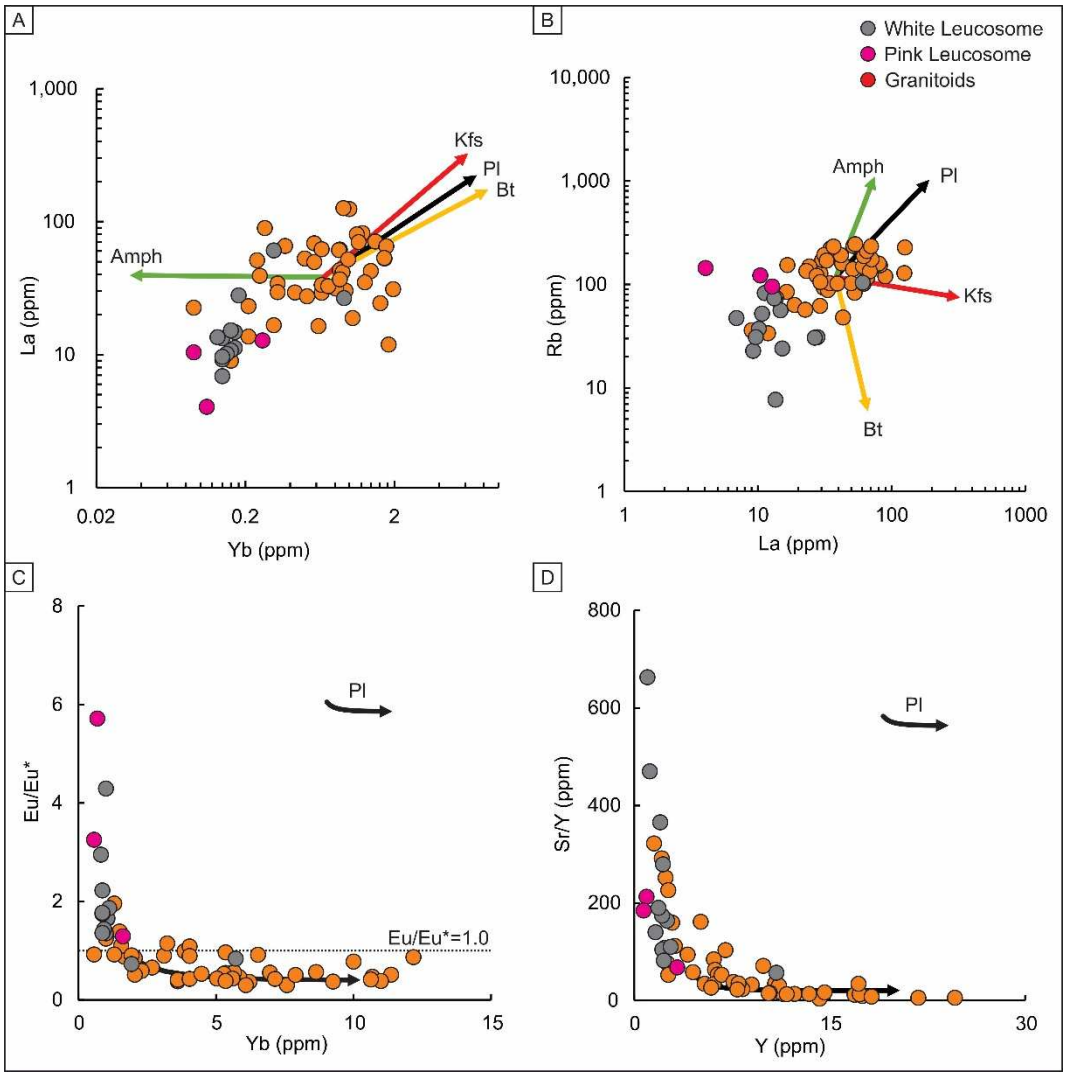

Figure 10. (**A**,**B**) Log–log vector diagrams with amphibole, biotite, K-feldspar, and plagioclase vectors. (**C**) Eu/Eu* vs. Yb plot with plagioclase vector. The dashed line marks the limit between positive (Eu/Eu* > 1) and negative (Eu/Eu* < 1) Eu anomaly; (**D**) Sr/Y vs. Y plot with plagioclase vector.

7. LA-ICP-MS U-Pb Zircon Geochronology

A set of four samples was selected for LA-ICP-MS U-Pb zircon geochronology. The samples include (i) a hercynite metadiorite (1H4; site 1 in Figure 1); (ii) a white leucosome of a schlieren diatexite (1G1; site 1 in Figure 1); (iii) a white leucosome of a schollen diatexite

(3A1; site 2 in Figure 1); and (iv) a pink leucosome that crosscuts the schlieren diatexite from which sample 1G1 was collected (site 1 in Figure 1). Sample (i) encompasses a syntectonic granitoid. Samples (ii) to (iv) are leucosomes of the migmatites of the Xingu Complex. Analytical data and uncertainties are shown in Table 2.

Table 2. Geochronological data of the hercynite metadiorite (1H4) and white (3A1 and 1G1) and pink (1J1) leucosomes of the Xingu Complex.

Spots	Comm. 206 (%)	U (ppm)	Th (ppm)	Th/U	$^{207}Pb/^{235}U$	1σ	$^{206}Pb/^{238}U$	1σ	$^{207}Pb/^{206}Pb$ Age (Ma)	2σ (Ma)	% Conc.
Hercynite Metadiorite (Sample 1H4)											
1H4_1	0.02	189.1	137.8	0.73	16.17	0.23	0.564	0.008	2883	11	100.1
1H4_2	0.02	337.0	138.9	0.41	15.81	0.25	0.559	0.011	2864	15	99.8
1H4_3	0.03	189.2	136.1	0.72	16.04	0.20	0.564	0.007	2860	10	100.9
1H4_4	0.01	397.0	150.0	0.38	15.35	0.22	0.551	0.008	2842	11	99.3
1H4_5	0.02	338.7	218.3	0.64	16.27	0.20	0.569	0.008	2870	9	101.0
1H4_6	0.02	349.0	220.3	0.63	16.10	0.19	0.568	0.007	2855	10	101.5
1H4_7	0.02	285.1	230.1	0.81	16.04	0.22	0.560	0.008	2869	11	99.7
1H4_8	0.02	284.0	204.0	0.72	15.65	0.22	0.560	0.009	2823	12	101.5
1H4_9	0.03	223.7	139.3	0.62	16.45	0.23	0.567	0.009	2893	12	99.9
1H4_10	0.03	220.8	142.2	0.64	16.05	0.23	0.561	0.009	2875	12	99.7
1H4_11	0.02	261.7	204.6	0.78	15.65	0.21	0.553	0.009	2869	12	98.7
1H4_12	0.01	492.0	261.8	0.53	16.45	0.29	0.571	0.010	2899	14	100.2
White Leucosome (Sample 3A1)											
3A1_1	0.09	75.6	354.5	4.69	15.68	0.32	0.556	0.012	2866	18	99.1
3A1_2	0.08	79.2	346.5	4.38	15.78	0.27	0.561	0.010	2851	15	100.7
3A1_3	0.06	116.0	715.0	6.16	15.73	0.29	0.558	0.012	2871	18	99.2
3A1_4	0.04	136.2	246.8	1.81	15.64	0.28	0.558	0.011	2847	16	100.2
3A1_5	0.14	45.3	181.8	4.01	15.86	0.31	0.557	0.011	2873	18	99.4
3A1_6	0.11	58.1	240.3	4.14	15.82	0.25	0.560	0.010	2860	16	99.9
3A1_7	0.16	39.4	180.8	4.59	15.80	0.28	0.557	0.011	2881	17	98.6
White Leucosome (Sample 1G1)											
1G1_1	0.01	302.0	308.0	1.02	15.52	0.23	0.558	0.009	2842	11	100.6
1G1_2	0.01	284.2	231.8	0.82	15.86	0.23	0.557	0.009	2878	10	99.3
1G1_3	0.02	210.6	198.4	0.94	15.39	0.16	0.555	0.007	2857	8	99.5
1G1_4	0.01	335.7	337.1	1.00	15.71	0.22	0.560	0.009	2854	10	100.6
1G1_5	0.02	268.7	173.9	0.65	15.23	0.21	0.547	0.008	2822	10	99.7
1G1_6	0.02	217.1	200.4	0.92	15.69	0.17	0.560	0.007	2856	8	100.2
1G1_7	0.02	218.4	171.0	0.78	15.47	0.23	0.552	0.009	2855	11	98.9
1G1_8	0.02	250.4	226.8	0.91	15.69	0.18	0.556	0.007	2854	9	100.0
1G1_9	0.01	302.8	244.8	0.81	15.22	0.20	0.545	0.008	2845	11	98.7
1G1_10	0.02	279.5	274.2	0.98	15.69	0.15	0.557	0.006	2859	8	99.7
1G1_11	0.02	197.8	197.7	1.00	15.73	0.18	0.561	0.007	2851	9	100.5
1G1_12	0.02	232.8	194.5	0.84	15.65	0.17	0.554	0.007	2857	9	99.5
1G1_13	0.03	153.2	132.7	0.87	15.71	0.18	0.557	0.008	2863	10	99.5
1G1_14	0.02	287.4	257.2	0.89	15.62	0.26	0.560	0.010	2847	11	100.6
1G1_15	0.02	270.4	205.1	0.76	16.51	0.24	0.568	0.009	2899	11	99.9
1G1_16	0.02	229.9	215.8	0.94	15.93	0.23	0.565	0.009	2856	11	101.2
1G1_17	0.01	335.0	278.1	0.83	15.65	0.14	0.559	0.006	2851	8	100.4
1G1_18	0.01	373.0	149.5	0.40	15.60	0.18	0.558	0.007	2845	9	100.7
Pink Leucosome (Sample 1J1)											
1J1_1	0.02	287.5	212.2	0.74	15.46	0.28	0.542	0.012	2875	14	97.0
1J1_2	0.04	139.4	89.6	0.64	15.96	0.22	0.568	0.009	2833	14	102.3
1J1_3	0.03	186.4	119.3	0.64	16.17	0.23	0.567	0.009	2885	12	100.4
1J1_4	0.02	304.7	156.8	0.51	15.21	0.29	0.537	0.011	2860	16	96.9
1J1_5	0.01	512.0	137.1	0.27	16.02	0.21	0.566	0.008	2861	10	100.9
1J1_6	0.03	192.7	121.7	0.63	15.94	0.21	0.560	0.008	2862	11	100.1
1J1_7	0.02	328.0	186.9	0.57	16.10	0.20	0.566	0.008	2868	10	100.7
1J1_8	0.02	387.0	162.5	0.42	16.02	0.25	0.565	0.010	2864	12	100.5
1J1_9	0.03	218.6	90.0	0.41	16.01	0.21	0.561	0.009	2867	11	100.1
1J1_10	0.02	307.0	123.9	0.40	15.43	0.25	0.555	0.010	2836	13	100.2
1J1_11	0.03	179.2	124.6	0.70	15.96	0.22	0.560	0.008	2854	11	100.3
1J1_12	0.04	152.5	96.6	0.63	15.24	0.20	0.542	0.008	2846	12	98.1

7.1. Hercynite Metadiorite (Sample 1H4)

Zircon grains of the hercynite metadiorite (sample 1H4) are dominantly murky pink colored, subidiomorphic, and ovoid. Crystals may lack internal textures or present weak oscillatory zoning with xenocrystic darker cores (Figure 11A–C). The crystal length varies

from 122 to 334 µm, with elongation from 1 to 2, except for one highly prismatic grain, in which elongation is around 5. Th/U ratios range from 0.38 to 0.81 (Table 2). Twelve spot analyses provided a Concordia age of 2876 ± 13 Ma (MSWD = 1.3, Figure 12A). The sample 1H4 shows $^{207}Pb/^{206}Pb$ ages ranging from 2823 ± 12 to 2899 ± 14 Ma.

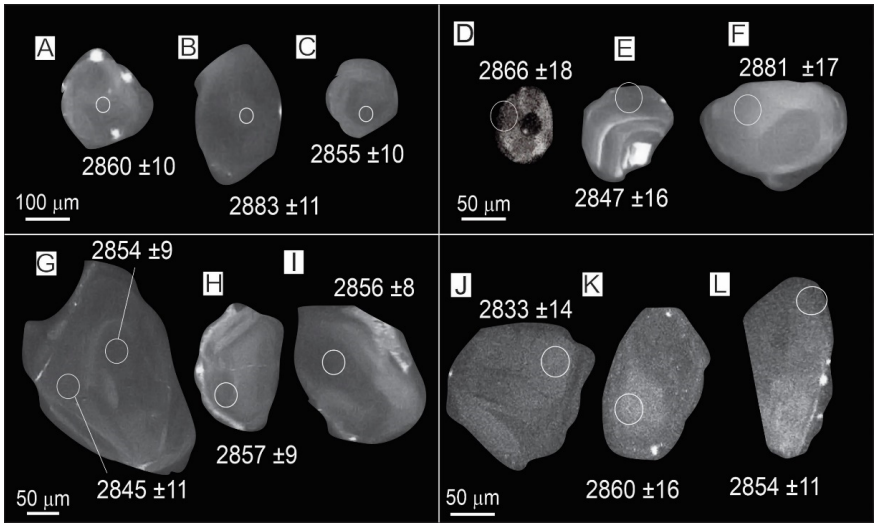

Figure 11. CL images of zircon grains of the hercynite metadiorite ((**A**–**C**); sample 1H4; site 1 in Figure 1); the white leucosome of schlieren diatexite ((**D**–**F**); sample 3A1; site 2 in Figure 1), the white leucosome of schollen diatexite ((**G**–**I**); sample 1G1; site 1 in Figure 1); and pink leucosome ((**J**–**L**); sample 1J1; site 1 in Figure 1). $^{207}Pb/^{206}Pb$ ages are indicated at the analyzed spots.

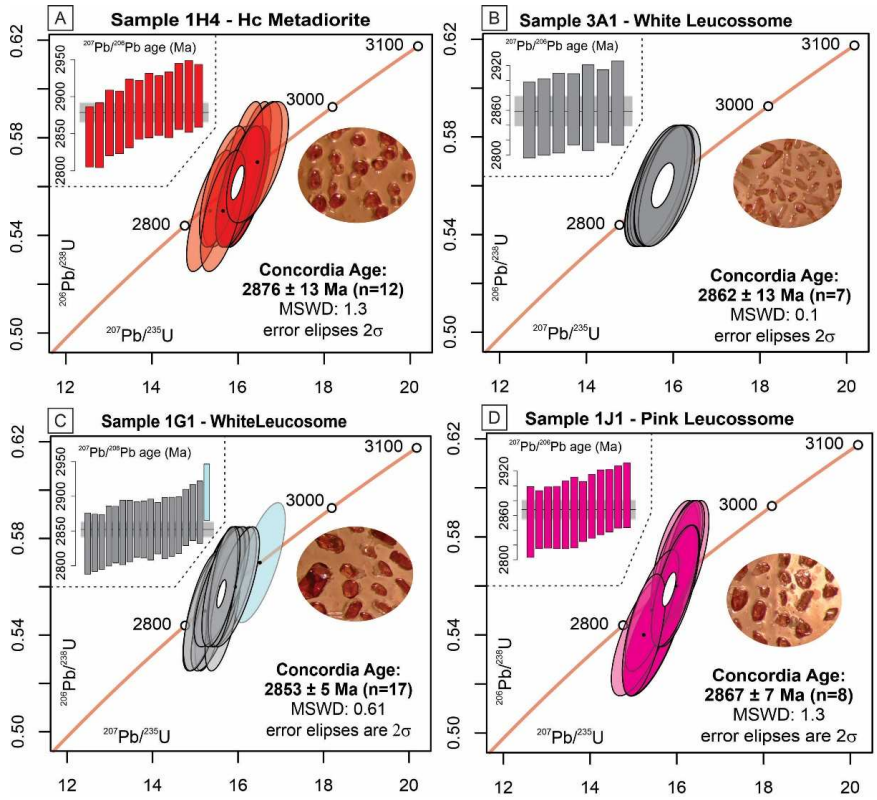

Figure 12. $^{206}Pb/^{238}U$ vs. $^{207}Pb/^{235}U$ diagrams of zircons of the rocks analyzed by U–Pb LA-ICP-MS and zircon grains aspect under the magnifier for (**A**) hercynite metadiorite (sample 1H4; site 1 in Figure 1); (**B**) white leucosome of a schollen diatexite (sample 3A1; site 1 in Figure 1); (**C**) white leucosome of a schlieren diatexite (sample 1G1; site 2 in Figure 1); (**D**) pink leucosome that crosscut a schlieren diatexite (sample 1J1; site 1 in Figure 1).

7.2. White Leucosome (Sample 3A1)

Zircon grains of sample 3A1 are light-pink translucent to white, subidiomorphic, and have oval or prismatic shapes with sub-rounded terminations. Zircon fragments are also observed. The crystal length ranges from 48 to 162 µm, with an elongation ratio from 1 to 2. Grains show no internal texture, concentric oscillatory, or vague sector zoning (Figure 11G–I). The Th/U ratio ranges from 1.81 to 6.16, reflecting low U concentration (39.4–136.2 ppm; Table 2). Seven spot analyses yielded a concordia age of 2862 ± 13 Ma (MSWD = 0.1; Figure 12B). The $^{207}Pb/^{206}Pb$ age in the sample ranges from 2847 ± 16 to 2881 ± 17 Ma.

7.3. White Leucosome (Sample 1G1)

Zircon grains of sample 1G1 are pink, idiomorphic to subidiomorphic, and either oval-shaped or prismatic, with rounded to flat terminations. Crystal lengths range from 60 to 262 µm, with a length/width ratio from 1 to 3. The Th/U ratio ranges from 0.4 to 1.02 (Table 2). Most grains do not present an internal texture (Figure 11D–F), though discrete resorption shapes and oscillatory zoning are identified in some grains. Seventeen spot analyses provided a concordant age of 2853 ± 5 Ma (MSWD = 0.61; Figure 12C). A single-spot analysis with a $^{207}Pb/^{206}Pb$ age of 2899 ± 11 Ma (Table 2) was identified as an outlier within the group of analyses, with $^{207}Pb/^{206}Pb$ age ranging from 2822 ± 10 and 2878 ± 10 Ma (Table 2). While this analysis was excluded from the age calculation, it is still shown in the diagram (Figure 12C).

7.4. Pink Leucosome (Sample 1J1)

Zircon grains of sample 1J1 are homogenous translucent pink or present a white core overgrown by a light-pink tip. Crystals are subidiomorphic to xenomorphic with highly resorbed or ovoid shapes, though prismatic variations exist with pyramidal to sub-rounded terminations. Most grains do not display an internal texture, but some are core-and-rim-structured, with brighter rims (Figure 11J–L). The crystal length ranges from 70 to 162 µm, with an aspect ratio from 1 to 3. Th/U ratios range from 0.27 to 0.74. Twelve spot analyses yielded a concordant age of 2867 ± 7 Ma (MSWD = 1.3; Figure 12D). The $^{207}Pb/^{206}Pb$ ages in the sample 1J1 range from 2833 ± 14 to 2885 ± 12 Ma.

8. Discussion

High-grade metamorphism and partial melting events played a crucial role in the Archean crustal evolution of the Carajás Domain in the Amazonian Craton. The genesis of TTG rocks, which make up the protoliths of the orthogneisses in the Xicrim-Cateté Orthogranulite and Xingu Complex, as well as the majority of the Carajás Domain crust, is linked to the incongruent partial melting of metabasites at the base of island arcs, as proposed by Delinardo-Silva et al. [9].

The Xicrim-Cateté Orthogranulite records UHT metamorphism and early episodic dehydration partial melting at ca. 3.06 and 2.93 Ga [9]. These processes resulted in migmatites with pargasite-bearing mafic granulite paleosome, neosome with peritectic enstatite, diopside, and plagioclase, and residual amphibole-free mafic granulite. The underplating of mantle melts enhanced the episodical partial dehydration melting of the lower mafic crust melts, as indicated by the εHf values (−2.2 to +1.2) of zircon neosome [9]. In this scenario, the TTG protoliths of the Xingu orthogneisses enclose the liquids expelled from the lower crust during the episodes of the partial dehydration melting of the Xicrim-Cateté Orthogranulite.

At ca. 2.89 to 2.84 Ga, the Xicrim-Cateté Orthogranulite and Xingu Complex rocks were deformed and partially melted [9–12]. The following discussion explores the nature and implications of these Late Mesoarchean processes for the Carajás Province.

8.1. Mechanisms of the Partial Melting in the Xicrim-Cateté Orthogranulite and Xingu Complex in the Late Mesoarchean

The nature of the Late Mesoarchean partial melting in the orthogneisses of the Xicrim-Cateté Orthogranulite and Xingu Complex can be traced through both macroscopic and microscopic features. The macroscopic features provide insight into the scale of the event, while the microscopic features reveal the mechanisms of partial melting in the oldest orthogneisses of the Carajás Domain. The textures of the paleosome and neosome provide diverse information, yet they remain consistent in terms of the partial melting mechanisms.

The paleosome of the migmatites from the Xicrim-Cateté Orthogranulite and Xingu Complex exhibits a common textural feature observed in the diopside–enstatite orthogneiss, biotite orthogneiss, and hornblende orthogneiss: xenomorphic crystals of K-feldspar (Figure 4D–F), plagioclase (Figure 4F,G), or quartz (Figure 4G) along the grain boundaries of the rock-forming phases. Similar xenomorphic grains are also observed in the biotite-bearing melanosome of these migmatites (Figure 6E,F). These grains typically show a cuspate shape or form films along the grain boundaries of the rock-forming phases, with minimal dihedral angles at their corners. These grains are interpreted as pseudomorphs of pores filled by the melt that was not expelled from the migmatite [58–60]. These authors also emphasize that melt pseudomorphs often differ from the pore wall phases, such as feldspars of different compositions (e.g., plagioclase in pores with walls defined by orthoclase or quartz, Figure 4D).

The phases in the pore walls around melt pseudomorphs may contain relicts of corroded boundaries [59,60]. In the paleosome and in the biotite-bearing melanosome of the migmatites from the Xicrim-Cateté Ortogranulite, these relicts are visible in plagioclase and quartz grains (Figures 4D and 6E). The preserved corroded boundaries are also observed in quartz, orthoclase, plagioclase, and biotite crystals in the paleosome of the migmatites from the Xingu Complex (Figure 4E,F). These corroded boundaries suggest that these phases were part of the reactant assemblage in the melting reactions [58–60]. The accumulation of biotite (Figures 5F and 6F) and plagioclase (Figure 6F) in the biotite-bearing melanosome suggests that orthoclase and quartz were mostly consumed during partial melting reactions.

The patch morphology (Figures 2A and 5B) in the amphibolitic layers (paleosome) of the migmatites from the northeastern portion of the Xingu Complex indicates the local presence of hornblende as part of the neosome assemblage. In Figure 4G, relicts of corroded boundaries are not observed in hornblende crystals from the pore walls in the paleosome. Instead, the grains exhibit inclusions and have idioblastic to subidioblastic shapes (Figure 4G). In the melanosome, hornblende grains form perfectly idioblastic crystals that grow toward the leucosome and eventually show a symplectic texture with quartz (Figure 6G,H). According to the criteria of Vernon [60], these textures suggest the existence of two generations of hornblende: (i) residual crystals in the paleosome with overgrowth boundaries that define an idioblastic shape and (ii) solid products of partial melting reactions. The symplectic texture provides evidence of back-reactions between the cooling melt and peritectic grains [60].

The large biotite grains in the melanosome, which surrounds the leucosome layers identified in the diopside–enstatite orthogneiss of the Xicrim-Cateté Orthogranulite, highlight the complexity of partial melting in these rocks. Patches of neosome were not detected, and the leucosome layers are hololeucocratic (Figure 5A), with a very low proportion of biotite and other mafic minerals (~3%). The biotite grains exhibit corroded boundaries in the pore walls of melt pseudomorphs defined by xenomorphic quartz grains (upper

right in Figure 6E) and are also included by them (center in Figure 6E). Additionally, biotite crystals replace diopside and enstatite grains in the orthogneiss (Figures 4C and 6E). In this context, biotite grains may have formed and grown during the hydration of the diopside–enstatite orthogneiss. The hydration was diachronous to partial melting, which also locally consumed biotite and plagioclase. The phases enclose the abundant residual assemblage in the melanosome, which lacks orthoclase, the subordinate feldspar of the paleosome (Figure 6E).

The leucosomes of the migmatites of the Xicrim-Cateté Orthogranulite and Xingu Complex are commonly hololeucocratic, with small proportions of mafic phases (Figure 5A–D). The white and pink types show variations in the modal proportion of plagioclase (up to 43 vol. % in the white and ~30 vol. % in the pink) and K-feldspar (up to 26 vol. % in the white and ~35 vol. % in the pink). The leucosome layers form aggregates of quartz, plagioclase, K-feldspar, and other phases of minor abundance (e.g., apatite, biotite; Figure 6A–D), which resemble the composition of granitoids and are the most reliable criteria of the former melt presence (i.e., [60]). In addition, other specific criteria are also detected, such as (i) the idioblastic shape of plagioclase (Figure 6A,B) and microcline (Figure 6B) against quartz; (ii) the microgranophyric intergrowth of quartz and orthoclase (Figure 6A) and quartz and albite (Figure 6D); (iii) large melt pseudomorphs define by microcline crystals with quartz and plagioclase inclusions (Figure 6D).

The patch morphology in mafic bands of the hornblende orthogneiss, along with the melt pseudomorphs in the diopside–enstatite, biotite, and hornblende orthogneiss, are reliable indicators of melt generation during anatexis [56–58,66]. Variations in textures and mineral assemblages in the paleosome and neosome (leucosome and melanosome) suggest that (i) the reactants in the partial melting reactions of felsic orthogneiss were quartz, plagioclase, orthoclase, and biotite; (ii) the melting reactions in the felsic orthogneisses do not generate solid products; and (iii) the partial melting of the hornblende orthogneiss focused on the fertile felsic hololeucocratic bands but also affected the mafic bands, allowing peritectic hornblende to form as a solid product of the reactions.

The features of the migmatites mentioned above are typical of water-fluxed partial melting (e.g., [5,67–70]). The textures and mineral assemblages observed in the migmatites of the Xingu Complex and Xicrim-Cateté Orthogranulite suggest the following water-fluxed partial melting reactions: (i) K-feldspar + quartz + plagioclase + H_2O = melt; (ii) biotite + K-feldspar + quartz + H_2O = melt; and (iii) hornblende$_1$ + quartz + H_2O = hornblende$_2$ + melt. Based on reaction (ii), Watkins et al. [71] constrained the wet solidus of TTG orthogneiss to 680–690 °C, at pressures of 6 kbar. Lapin and Hollister [67] suggested that reaction (iii) produces granitic melt in the pressure and temperature interval of 675–750 °C and 6 to 8 kbar. In conclusion, the data suggest that water-fluxed partial melting occurred in the upper amphibolite facies of the orthogneisses of the Xicrim-Cateté Orthogranulite and Xingu Complex.

8.2. The Amplitude of the Late Mesoarchean Anatetic Event and the Relationship with Syntectonic Granitoids

The migmatites are widespread in the Carajás Domain. Figure 1 shows sites 1 to 9, in the western and eastern parts of the Carajás Domain, where migmatite morphologies (Figure 2A–E) and their constituent parts (Figures 3A–E and 5A–G) are found, described, and distinguished from other Archean lithotypes (Figure 6A–E). Currently, most of these migmatites are included in the Xingu Complex, with a smaller portion found in the Xicrim-Cateté Orthogranulite (Figure 1). The previous section demonstrated how pervasive partial melting at upper amphibolite facies conditions was largely influenced by the influx of water into a hot middle crust.

Tracing the fluid source is a very complex task that requires further studies. Nevertheless, contextualizing the partial melting in the Mesoarchean geological evolution of the Carajás Domain may give some clues about this process. The leucosomes are structurally controlled (e.g., Figures 2B, 3D, 4E and 5C,F) by low- to high-angle ENE-WNW structures, suggesting that the partial melting event at ca. 2.87 to 2.85 Ga (this study; [10]) was coeval with the development of the broad system of linked thrust and sinistral strike-slip shear zones resulting in the Mesoarchean penetrative ductile fabric formation [10,19,20]. The shear zones juxtaposed gneisses, granulites, and greenstone belt sequences with metabasites, meta-ultramafic rocks, metapsamites, and metapelites [19,20,33]. The ductile fabric development was also coeval to the emplacement of granitoids (Figure 7B,D). Considering the ways that water can ingress into the hot lower and middle crust [72], the hypothesis of water-fluxed melting may involve (i) the influx of fluids released by underthrusted rocks at depth (e.g., greenstone belt sequences) and channelized into shear zones; (ii) the emplacement of water-rich magmas out of equilibrium with the water-undersaturated host rocks.

The Mesoarchean (>2.97 Ga; [36]) lenses of greenstone belts juxtaposed with the orthogneisses, granulites, and migmatites of the Xicrim-Cateté Orthogranulite and Xingu Complex (Figure 1) stand out as a significant source of fluids. These metavolcanic-sedimentary sequences contain water-rich rocks, including amphibole- and chlorite-bearing metaultramafic schists, serpentinites, amphibolites, and biotite–muscovite schists with or without garnet (e.g., [33]). Their peak metamorphic conditions, ranging from greenschist to lower amphibolite facies [33,73], are highly favorable for the release of large volumes of fluids due to devolatilization reactions [74], which likely played an essential role in water-fluxed melting within the basement orthogneisses.

Sanukitoid-affinity magmatism (ca. 2.92–2.87 Ga; [17,18]) in the Carajás Province is characterized by high water contents (>6 wt%; [15,27,75,76]), and sanukitoid emplacement was roughly coeval to partial melting. As the emplacement of sanukitoids appears to be controlled by regional structures (Figure 7B), the water released by these intrusions could percolate and promote the partial melting of host rocks. The intrusive hercynite metadiorite is an intermediate, hornblende-rich (~20 vol. %; Figure 8A) granitoid that is also intrusive in the Xingu Complex (Figure 7A), although its source and geochemical affinity remain unknown. The presence of amphibole instead of pyroxene suggests a higher water content in the magma (e.g., [77]), which could have been partially released into the host orthogneiss of the Xingu Complex. This may explain the higher melt fraction in the migmatite adjacent to the metadiorite, which exhibits a schollen morphology. The hercynite metadiorite yielded a crystallization age of 2876 ± 13 Ma (MSWD: 1.3; Figure 12A), predating the partial melting recorded in the proximal white and pink leucosomes at 2853 ± 5 Ma (MSWD: 0.61; Figure 12C) and 2867 ± 7 Ma (MSWD: 1.3; Figure 12D). The zircon population of the hercynite metadiorite shows a negative skew in the weighted mean plot, with a tail toward younger $^{207}Pb/^{206}Pb$ ages (Figure 12A). This feature may suggest that some lead loss occurred (e.g., [78]) during the interaction with the nearby leucosomes that locally crosscut the metadiorite (Figure 7A). An outlier zircon grain with a $^{207}Pb/^{206}Pb$ age of 2899 ± 11 Ma, found in the population of the white leucosome (sample 1G1; Figure 12C), reinforces the interpretation of the interaction between the products of partial melting and the metadiorite. The protoliths of the partially melted orthogneisses of the Xingu Complex have crystallization ages older than ca. 2.94 Ga. Until now, only metamorphic rims, rather than metamorphic zircon grains, have been described in these rocks, ruling out the hypothesis of inherited zircon grains from the paleosome.

The syntectonic granitoids encompass a diverse group of rocks that were emplaced during the regional deformation of the Carajás Domain in the Mesoarchean, as revealed

by their structures (Figure 7B,D) and microstructures (Figure 8D,E). Nevertheless, the diffuse contact between a biotite granite and orthogneiss of the Xingu Complex shown in Figure 7C resembles the schollen morphology of the migmatites depicted in Figure 2D,E. In fact, these two outcrops (Figures 2D,E and 7C) exemplify the gradual transition between the migmatites and the Mesoarchean (ca. 2.87 Ga) Nova Canadá Granodiorite [16], supporting its characterization as an anatectic granite derived from the partial melting of the orthogneiss of the Xingu Complex. The rough superimposition of the ages of this unit and the white and pink leucosome, which were dated by Machado et al. [10] at ca. 2.86 Ga and, in this study, at 2853 ± 5 Ma (MSWD: 0.61; Figure 12C), 2862 ± 13 Ma (MSWD: 0.1; Figure 12B), and 2867 ± 7 Ma (MSWD: 1.3; Figure 12D), also reinforce this hypothesis. Other syntectonic granitoids, chemically and isotopically similar to the Nova Canadá Granodiorite, exhibit crystallization ages ranging from ca. 2.88 to 2.83 Ga [13,15,25], overlapping with the leucosome ages as well. However, the contacts of these granitoids are often transposed by shear zones developed during the Neoarchean (e.g., [19]). Their commonly foliated boundaries (Figure 7D) favor strain localization [79], which erased important information about potential genetic relationships with the older gneissic basement.

In this context, correlating lithochemical data from these syntectonic granites and leucosomes was an essential complement to the geochronological information. Classification diagrams show that leucosomes and granitoids are compositionally similar (Figure 9A) and share comparable magmatic affinities (Figure 9B–E). The multi-element rare-earth diagram further highlights the geochemical similarities between leucosomes and granitoids, both of which are LREE-enriched and HREE-depleted (Figure 9F). Given the lithochemical dataset and the geochronological information, it is reasonable to conclude that leucosomes and granitoids may share the same source. However, Lu/Hf and Sm/Nd data for the leucosomes are needed to strengthen this conclusion. The diagram in Figure 9F highlights an important difference between the leucosomes and granitoids: variations in the content of Eu, Sm, and Nd, which define negative anomalies ($Eu/Eu^* < 1$) in the granitoids and positive anomalies ($Eu/Eu^* > 1$) or no anomaly ($Eu/Eu^* = 1$) in the leucosomes (Figure 9F; Table 1).

The log–log vector diagrams and binary diagrams of Sr/Y vs. Y and Eu/Eu* vs. Yb were developed to address this. The modeling is based on two main assumptions: (i) the magma was not completely expelled from the source, as indicated by the migmatite morphologies (e.g., Figures 2A–C, 4D–G and 5A–E); and (ii) crystal fractionation occurred in the leucosome prior to melt movement, as indicated by the idiomorphic crystals of plagioclase and K-feldspar (e.g., Figure 6A,B). The evolving trends of leucosome and granitoid samples displayed in the diagrams of Figure 10A,D suggest that plagioclase controlled the fractionation of magma, with only a minor influence from K-feldspar. Both phases have high partition coefficients for Eu in intermediate and felsic melts (Pl: 3.80; Kfs: 3.30; [54]). Hence, their early crystallization likely caused Eu/Eu* ratio variations between leucosomes and granitoids. Positive and negative Eu anomalies characterize the influence of plagioclase fractional crystallization—or its presence in the residuum—on the retained ($Eu/Eu^* > 1$) or expelled ($Eu/Eu^* < 1$) fractions of anatectic liquids in several migmatite–granite terrains, serving as an important tool for characterizing source-to-sink connections (e.g., [3,68,80,81]). In summary, the lithochemical data also support the leucosome–granite connection suggested by field and U-Pb geochronological data, indicating that the crustal-derived syntectonic granitoids may have formed from anatectic liquids produced by the partial melting of TTG orthogneisses from both the Xicrim-Cateté Orthogranulite and the Xingu Complex and, locally, from the mafic layers of the latter.

8.3. Geodynamic Implications for the Crustal Evolution and Metallogenesis of the Carajás Province

The mechanisms of the generation and crustal evolution of the Carajás Province during the Mesoarchean (ca. 3.0–2.8 Ga) are intensively debated in the literature. Some authors support the accretionary-to-collisional orogenic model [9,12,15,17,26,28], while others propose drip tectonics or sagduction models [21,22].

Vertical tectonics are proposed for the Carajás Province due to the absence of petrotectonic associations typical of modern subduction (e.g., blueschists, eclogites, UHP rocks, ophiolites) and similarities in the dome-and-keel architecture of the southern Rio Maria Domain [21] and other cratons (e.g., Pilbara; [82,83]), where this model is commonly adopted. However, gneiss domes surrounded by metasedimentary and metavolcanic rocks are found in the cores of orogenic belts across different geological eras, including the Phanerozoic (e.g., [84]). Even in the Archean, the nature of this architecture is debated and often attributed to convergent settings [85]. The Rio Maria Domain lacks sufficient structural data to enable a comprehensive regional understanding of the origin of its dome-and-keel architecture. Additionally, geochemical, geochronological, and Sm-Nd data [26,28] strongly suggest that Rio Maria terrains evolved through an accretionary and collisional orogeny.

The Carajás Domain contains several elongated Mesoarchean (2.92 to 2.83 Ga) syntectonic granitoids aligned with the general ENE-WNW gneissic foliation of the ancient (ca. 3.0 to 2.93 Ga) basement orthogneisses [9]. This structure defines the ductile fabric of the basement, as described by Pinheiro and Holdsworth [19]. Thus, the typical architecture of vertical tectonics is absent in the Carajás Domain. In addition, geochemical, geochronological, and Lu-Hf (εHf of −2.2 to +1.2, and T_{DM} of 3.4 to 3.2 Ga) and Sm-Nd (εNd of −4.09 to +2.75, and T_{DM} of 3.3 to 2.9 Ga) data strongly support an accretionary-to-collisional orogenic model [9,13]. The geodynamic processes related to the crustal evolution of the Carajás Domain also favored the formation of magmatic–hydrothermal copper deposits during the Mesoarchean, which are typical of convergent settings (e.g., ca. 2.89 Ga; Hades and Hades NE; [46]).

This study provides new insights into the geodynamic evolution of the Carajás Domain, linking it to a convergent setting. It connects the emplacement of water-rich sanukitoids [18,27,75,76], which were extracted from the mantle previously metasomatized by subduction processes [9,12,17], to the widespread partial melting of the overriding Carajás plate. Thus, the partial melting observed at ca. 2.87 to 2.85 Ga ([10]; this study) likely occurred during the stacking of the Rio Maria (sinking) and Carajás (overriding) plates. The structural elements (e.g., gneissic foliation and shear zones) developed during the convergence between these larger crustal blocks channeled fluids from the devolatilization reactions of metaultramafic, metamafic, and metasedimentary rocks, as well as water-rich magmas, promoting the widespread partial melting event in the overriding plate. The migmatite morphologies (e.g., Figure 2B,C) and examples of plastic deformation in the leucosomes and granitoids (e.g., Figures 6C, 7D, and 8E) also indicate that partial melting took place under a high-magnitude stress regime. Thus, the petrotectonic assemblage of the Carajás Domain basement—featuring high-grade granulites, gneisses, migmatites, elongated granitoid bodies, including sanukitoids, and imbricated oriented greenstone belt lenses—is the typical core of an Archean orogenic belt [86,87].

Collectively, the data indicate that the continental crust evolution at Carajás involved high-grade metamorphic processes in the lower crust and coeval emplacement of granites in the middle crust. After the Rio Maria-Carajás collisional assembly at ca. 2.89–2.84 Ga, the extensional rebound following slab break-off could have been critical for the Neoarchean (ca. 2.77–2.73 Ga; [10,37]) extensive magmatism (e.g., Parauapebas LIP; [39]) and the later installation of the ca. 2.71–2.68 Ga IOCG hydrothermal deposits in the Carajás Province. According to Touret et al. [88], in such a scenario, the ascendent flow of CO_2-rich fluids

derived from the partial melting of the metasomatized mantle leads to tectonic instability, the development of megashear zones, and regional-scale albite and scapolite hydrothermal alteration, which are typically related to IOCG deposits in Carajás and worldwide.

According to Skirrow [89], a comprehensive review of the major IOCG metallogenic provinces around the world has shown that IOCG deposits are associated with extension in magmatic arcs (Andean type), as well as with orogenic and post-orogenic settings. In all these scenarios, subduction processes were crucial for the earlier metasomatism of the sub-continental lithospheric mantle, occurring as far back as 100 Ma before the IOCG deposit formation, as also reported by Groves et al. [90].

The post-orogenic geodynamic setting was also proposed for the supergiant Olympic Dam IOCG deposit in the Gawler Craton, Austrália, by Skirrow et al. [91] and Skirrow [89]. At the Olympic Gawler Craton, previous subduction at ca. 1610 Ma resulted in mantle metasomatism, followed by delamination and major foundering of the metasomatized subcontinental lithospheric mantle. This caused a tectonic switch from compression to extension and allowed for widespread mantle and crustal melting, resulting in voluminous felsic-dominated bimodal igneous activity at ca. 1595–1586 Ma, recognized as the Gawler large igneous province [92,93]. The magmatic evolution was followed by extensive alkaline hydrothermal alteration and IOCG deposit formation.

Thus, considering a mineral system approach, the Mesoarchean geodynamic setting was critical for the formation of ca. 2.89 Ga magmatic–hydrothermal copper deposits [46] in a convergent setting and the Neoarchean iron oxide–copper–gold deposits related to the post-collisional extensional rebound.

9. Conclusions

The mechanism of the partial melting of the Xicrim-Cateté Orthogranulite and Xingu Complex was the influx of water into a hot lower to middle crust. This is evidenced by the characteristics of melt pseudomorphs in the paleosome and their relationship with the reactant phase. The hypothesis is reinforced by the assemblage of the neosome, which lacks solid products of melting reactions or contains peritectic hornblende. These are characteristics of melting reactions at upper amphibolite facies related to the wet solidus of the orthogneisses: (i) K-feldspar + quartz + plagioclase + H_2O = melt; (ii) biotite + K-feldspar + quartz + H_2O = melt; and (iii) $hornblende_1$ + quartz + H_2O = $hornblende_2$ + melt.

Fluids released from metasedimentary rocks in greenstone belt sequences, as well as from water-rich sanukitoids (2.92–2.87 Ga) occurring as sheets in orthogneisses or crosscutting them as discordant intrusions, may be primarily responsible for this regional anatectic event. The migmatite–granite connection was suggested by locally preserved exposures showing a diffuse transition between schollen and schlieren migmatites and biotite granites of the Nova Canadá Granodiorite. This hypothesis was further supported by trends in leucosome and granitoids lithochemical data, which were established through plagioclase removal prior to melt extraction. The granitoids and leucosomes are chemically similar and show evolving trends controlled by plagioclase fractional crystallization, favoring a source-to-sink connection. In addition, the partial overlap of leucosomes of the migmatites at 2853 ± 5 Ma (MSWD: 0.61), 2862 ± 13 Ma (MSWD: 0.1), and 2867 ± 7 Ma (MSWD: 1.3) and granite (ca. 2.88–2.83 Ga; [13–17]) supports the migmatite–granite connection.

Despite the ongoing debate in the literature about the crustal evolution of the Carajás Province, significant evidence supports the accretionary-to-collisional orogenic model, including structural, geochemical, geochronological, Lu-Hf (εHf of −2.2 to +1.2, and T_{DM} of 3.4 to 3.2 Ga) and Sm-Nd (εNd of −4.09 to +2.75, and T_{DM} of 3.3 to 2.9 Ga) isotopic, and metallogenetic data. The pattern of migmatite morphologies and microstructures in leucosomes and granites suggests a high-amplitude stress regime related to the partial

melting event. Thus, the relationship between sanukitoids, migmatites, and crustal granites likely suggests the stacking of the overriding Carajás plate above the sinking Rio Maria plate, leading to the current configuration of the Carajás Province in the Late Mesoarchean.

The Mesoarchean geodynamic setting was crucial for the formation of ca. 2.89 Ga magmatic–hydrothermal copper deposits in a convergent setting and Neoarchean iron oxide–copper–gold deposits related to post-orogenic extensional rebound.

Supplementary Materials: The following supporting information can be downloaded at: https://www.mdpi.com/article/10.3390/min15030265/s1, Table S1: Compiled lithochemical data of the Mesoarchean syntectonic granitoids. Eu/Eu* ratios were calculated by the formula $Eu/\sqrt{Sm \cdot Gd}$, using values normalized by the C1 chondrite [62].

Author Contributions: Conceptualization, M.A.D.-S., L.V.S.M., C.P.N.M., J.F., T.J.S.S., S.D.S. and R.P.X.; formal analysis, M.A.D.-S. and J.F.; investigation M.A.D.-S., J.F. and S.D.S.; resources, L.V.S.M., C.P.N.M., T.J.S.S. and R.P.X.; data curation, M.A.D.-S. and J.F.; writing—original draft preparation, M.A.D.-S.; writing—review and editing, L.V.S.M., C.P.N.M., T.J.S.S. and R.P.X.; visualization, M.A.D.-S. and J.F.; supervision, L.V.S.M., C.P.N.M., T.J.S.S. and R.P.X.; project administration, L.V.S.M., C.P.N.M. and T.J.S.S.; funding acquisition, L.V.S.M., C.P.N.M. and T.J.S.S.. All authors have read and agreed to the published version of the manuscript.

Funding: This research was funded by FAEPEX/PRP/UNICAMP (grant 519.292–0045/15), INCT/Geociam (CNPq/FAPESPA/Petrobras 573733/2008-2), FAPESP (grant 2016/13162-7), and CNPq (grant 457689/2014-5; 310514/2022-3).

Data Availability Statement: The data presented in this study are available in the article and Supplementary Material.

Acknowledgments: We are grateful to the Geoscience Institute of the Federal University of Pará (UFPA), especially Davis Oliveira, for logistical support during fieldwork and to Britamil and Britalider staff for facilities in accessing quarries. We also thank laboratory technicians of the Geoscience Institute of the University of Campinas for their support during data acquisition. We are grateful to CAPES for the Master's and Ph.D. scholarships. L.V.S. Monteiro is a Research Fellow of CNPq (Conselho Nacional de Desenvolvimento Científico e Tecnológico-310514/2022-3) and acknowledges the continuous support.

Conflicts of Interest: The authors declare no conflict of interest.

References

1. Brown, M. Granites, Migmatites and Residual Granulites: Relationships and Processes. In *Working with Migmatites*; Mineralogical Association of Canada: Quebec City, QC, Canada, 2008; pp. 97–144.
2. Sawyer, E.W.; Cesare, B.; Brown, M. When the Continental Crust Melts. *Elements* **2011**, *7*, 229–234. [CrossRef]
3. Brown, C.R.; Yakymchuk, C.; Brown, M.; Fanning, C.M.; Korhonen, F.J.; Piccoli, P.M.; Siddoway, C.S. From Source to Sink: Petrogenesis of Cretaceous Anatectic Granites from the Fosdick Migmatite–Granite Complex, West Antarctica. *J. Petrol.* **2016**, *57*, 1241–1278. [CrossRef]
4. Korhonen, F.J.; Brown, M.; Grove, M.; Siddoway, C.S.; Baxter, E.F.; Inglis, J.D. Separating Metamorphic Events in the Fosdick Migmatite–Granite Complex, West Antarctica. *J. Metamorph. Geol.* **2012**, *30*, 165–192. [CrossRef]
5. Martini, A.; de Bitencourt, M.F.; Weinberg, R.F.; De Toni, G.B.; Lauro, V.S.N. From Migmatite to Magma—Crustal Melting and Generation of Granite in the Camboriú Complex, South Brazil. *Lithos* **2019**, *340–341*, 270–286. [CrossRef]
6. Sawyer, E.W. Disequilibrium Melting and the Rate of Melt-Residuum Separation During Migmatization of Mafic Rocks from the Grenville Front, Quebec. *J. Petrol.* **1991**, *32*, 701–738. [CrossRef]
7. Brown, M. Crustal Melting and Melt Extraction, Ascent and Emplacement in Orogens: Mechanisms and Consequences. *J. Geol. Soc. Lond.* **2007**, *164*, 709–730. [CrossRef]
8. Solar, G.S.; Brown, M. Petrogenesis of Migmatites in Maine, USA: Possible Source of Peraluminous Leucogranite in Plutons? *J. Petrol.* **2001**, *42*, 789–823. [CrossRef]

9. Delinardo da Silva, M.A.; Monteiro, L.V.S.; Santos, T.J.S.; Moreto, C.P.N.; Sousa, S.D.; Faustinoni, J.M.; Melo, G.H.C.; Xavier, R.P.; Toledo, B.A.M. Mesoarchean Migmatites of the Carajás Province: From Intra-Arc Melting to Collision. *Lithos* **2021**, *388–389*, 106078. [CrossRef]
10. Machado, N.; Lindenmayer, Z.; Krogh, T.E.; Lindenmayer, D. U-Pb Geochronology of Archean Magmatism and Basement Reactivation in the Carajás Area, Amazon Shield, Brazil. *Precambrian Res.* **1991**, *49*, 329–354. [CrossRef]
11. Pidgeon, R.T.; Macambira, M.J.B.; Lafon, J.-M. Th–U–Pb Isotopic Systems and Internal Structures of Complex Zircons from an Enderbite from the Pium Complex, Carajás Province, Brazil: Evidence for the Ages of Granulite Facies Metamorphism and the Protolith of the Enderbite. *Chem. Geol.* **2000**, *166*, 159–171. [CrossRef]
12. Marangoanha, B.; de Oliveira, D.C.; Dall'Agnol, R. The Archean Granulite-Enderbite Complex of the Northern Carajás Province, Amazonian Craton (Brazil): Origin and Implications for Crustal Growth and Cratonization. *Lithos* **2019**, *350–351*, 105275. [CrossRef]
13. Feio, G.R.L.; Dall'Agnol, R.; Dantas, E.L.; Macambira, M.J.B.; Santos, J.O.S.; Althoff, F.J.; Soares, J.E.B. Archean Granitoid Magmatism in the Canaã Dos Carajás Area: Implications for Crustal Evolution of the Carajás Province, Amazonian Craton, Brazil. *Precambrian Res.* **2013**, *227*, 157–185. [CrossRef]
14. Silva, L.R.; Oliveira, D.C.; Santos, M.N.S. Diversity, Origin and Tectonic Significance of the Mesoarchean Granitoids of Ourilândia Do Norte, Carajás Province (Brazil). *J. S. Am. Earth Sci.* **2018**, *82*, 33–61. [CrossRef]
15. Silva, L.R.; de Oliveira, D.C.; do Nascimento, A.C.; Lamarão, C.N.; de Arimatéia Costa de Almeida, J. The Mesoarchean Plutonic Complex from the Carajás Province, Amazonian Craton: Petrogenesis, Zircon U–Pb SHRIMP Geochronology and Tectonic Implications. *Lithos* **2022**, *432–433*, 106901. [CrossRef]
16. Leite-Santos, P.J.; do Nascimento, A.C.; De Oliveira, D.C.; da Silva, L.R.; Gabriel, E.O. Granodiorito Pantanal, Granodiorito Nova Canadá e Granito Velha Canadá: Dados Isotópicos De U–Pb–Hf–Nd–Sr e Implicações Para Os Processos de Crescimento e Retrabalhamento Crustal. In Proceedings of the 17 Simpósio de Geologia da Amazônia, Santarém, Brazil, 23–25 October 2023; Sociedade Brasileira de Geologia: Santarém, Brazil, 2023; pp. 377–382.
17. da Silva, L.R.; de Oliveira, D.C.; Galarza, M.A.; do Nascimento, A.C.; Marangoanha, B.; Marques, G.T. Zircon U–Pb–Hf Isotope and Geochemical Constraints on the Petrogenesis and Tectonic Setting of Mesoarchean Granitoids from the Carajás Province, Amazonian Craton, Brazil. *Precambrian Res.* **2023**, *398*, 107204. [CrossRef]
18. do Nascimento, A.C.; de Oliveira, D.C.; Gabriel, E.O.; Leite-Santos, P.J. Geology, Geochemistry and Zircon SHRIMP U–Pb Geochronology of Mesoarchean High-Mg Granitoids: Constraints on Petrogenesis, Emplacement Timing and Deformation of the Água Limpa Suite in the Carajás Province, SE Amazonian Craton. *J. Geol. Soc. Lond.* **2024**, *182*, jgs2024-098. [CrossRef]
19. Pinheiro, R.V.L.; Holdsworth, R.E. Evolução Tectonoestratigráfica Dos Sistemas Transcorrentes Carajás e Cinzeiro, Cinturão Itacaiúnas, Na Borda Leste Do Cráton Amazônico, Pará. *Rev. Bras. Geoci.* **2000**, *30*, 597–606. [CrossRef]
20. Araújo, O.J.B.; Maia, R.G.N. *Programa Levantamento Geológicos Básicos do Brasil, Folha Serra dos Carajás (SB.22-Z-A), Estado do Pará: Texto Explicativo*; Serviço Geológico do Brasil: Recife, Brazil, 1991.
21. Grandjean da Costa, F.; Araújo dos Santos, P.; Corrêa de Oliveira Serafim, I.C.; Lima Costa, I.S.; Roopnarain, S. From Mesoarchean Drips to Modern–Style Tectonics in the Carajás Province, Amazonian Craton. *J. S. Am. Earth Sci.* **2020**, *104*, 102817. [CrossRef]
22. Teixeira, N.A.; Campos, L.D.; de Paula, R.R.; Lacasse, C.M.; Ganade, C.E.; Monteiro, C.F.; Lopes, L.B.L.; Oliveira, C.G. de Carajás Mineral Province—Example of Metallogeny of a Rift above a Cratonic Lithospheric Keel. *J. S. Am. Earth Sci.* **2021**, *108*, 103091. [CrossRef]
23. Santos, J.O.S. Geotectônica Dos Escudos Das Guianas e Brasil-Central. In *Geologia, Tectônica e Recursos Minerais do Brasil*; Bizzi, L.A., Schobbenhaus, C., Viddotti, R.M., Gonçalves, J.H., Eds.; Serviço Geológico do Brasil: Brasilia, Brazil, 2003; pp. 169–222.
24. Vasquez, M.L.; Rosa-Costa, L.T. *Geologia e Recursos Minerais do Estado do Pará: Texto Explicativo do Mapa Geológico e Recursos Minerais do Estado do Pará*; Serviço Geológico do Brasil: Belém, Brazil, 2008.
25. Moreto, C.P.N.; Monteiro, L.V.S.; Xavier, R.P.; Amaral, W.S.; dos Santos, T.J.S.; Juliani, C.; de Souza Filho, C.R. Mesoarchean (3.0 and 2.86 Ga) Host Rocks of the Iron Oxide–Cu–Au Bacaba Deposit, Carajás Mineral Province: U–Pb Geochronology and Metallogenetic Implications. *Miner. Depos.* **2011**, *46*, 789–811. [CrossRef]
26. Souza, Z.S.; Potrel, A.; Lafon, J.-M.; Althoff, F.J.; Martins Pimentel, M.; Dall'Agnol, R.; de Oliveira, C.G. Nd, Pb and Sr Isotopes in the Identidade Belt, an Archaean Greenstone Belt of the Rio Maria Region (Carajás Province, Brazil): Implications for the Archaean Geodynamic Evolution of the Amazonian Craton. *Precambrian Res.* **2001**, *109*, 293–315. [CrossRef]
27. Oliveira, M.A.; Dall'Agnol, R.; Althoff, F.J.; da Silva Leite, A.A. Mesoarchean Sanukitoid Rocks of the Rio Maria Granite-Greenstone Terrane, Amazonian Craton, Brazil. *J. S. Am. Earth Sci.* **2009**, *27*, 146–160. [CrossRef]
28. de Almeida, J.A.C.; Dall'Agnol, R.; de Oliveira, M.A.; Macambira, M.J.B.; Pimentel, M.M.; Rämö, O.T.; Guimarães, F.V.; Leite, A.A.d.S. Zircon Geochronology, Geochemistry and Origin of the TTG Suites of the Rio Maria Granite-Greenstone Terrane: Implications for the Growth of the Archean Crust of the Carajás Province, Brazil. *Precambrian Res.* **2011**, *187*, 201–221. [CrossRef]

29. Feio, G.R.L.; Dall'Agnol, R.; Dantas, E.L.; Macambira, M.J.B.; Gomes, A.C.B.; Sardinha, A.S.; Oliveira, D.C.; Santos, R.D.; Santos, P.A. Geochemistry, Geochronology, and Origin of the Neoarchean Planalto Granite Suite, Carajás, Amazonian Craton: A-Type or Hydrated Charnockitic Granites? *Lithos* **2012**, *151*, 57–73. [CrossRef]
30. Monteiro, L.V.S.; Xavier, R.P.; de Souza Filho, C.R.; Moreto, C.P.N. Metalogênese Da Província Carajás. In *Metalogênese das Províncias Minerais Brasileiras*; da Silva, M.G., Rocha Neto, M.B., Jost, H., Kuyumjian, R.M., Eds.; Serviço Geológico do Brasil: Belo Horizonte, Brazil, 2014; pp. 43–92.
31. DOCEGEO Revisão Litoestratigráfica da Província Mineral de Carajás. *Província Carajás: Litoestratigrafia e Principais Depósitos Minerais*; do Doce, C.V.R., Ed.; Sociedade Brasileira de Geologia: Belém, Brazil, 1988; pp. 11–54.
32. Barros, C.E.D.M.; Macambira, M.J.B.; Barbey, P.; Scheller, T. Dados Isotópicos Pb-Pb Em Zircão (Evaporação) e Sm-Nd Do Complexo Granítico Estrela, Província Mineral De Carajás, Brasil: Implicações Petrológicas e Tectônicas. *Rev. Bras. Geociências* **2004**, *34*, 531–538. [CrossRef]
33. Sousa, S.D.; Monteiro, L.V.S.; de Oliveira, D.C.; Silva, M.A.D.; Moreto, C.P.N. O Greenstone Belts Sapucaia Na Região de Água Azul Do Norte, Província Mineral de Carajás: Contexto Geológico e Caracterização Petrográfica. In *Contribuições a Geologia da Amazônia*; Gorayeb, P.S.d.S., de Lima, A.M.M., Eds.; Sociedade Brasileira de Geologia: Belém, Brazil, 2015; Volume 9, pp. 317–338.
34. Costa, U.A.P.; Paula, R.R.; Silva, D.P.B.; Barbosa, J.P.O.; Silva, C.M.G.; Tavares, F.M.; Oliveira, J.K.M.; Justo, A.P. *Programa Geologia do Brasil—PGB. Mapa de Integração Geológico-Geofísica da Província Carajás. Escala 1:250.000*; Serviço Geológico do Brasil: Belém, Brazil, 2016.
35. De Avelar, V.G.; Lafon, J.-M.; Correia, F.C., Jr.; Macambira, E.M.B. O Magmatismo Arqueano Da Região de Tucumã-Província Mineral de Carajás: Novos Resultados Geocronológicos. *Rev. Bras. Geociências* **1999**, *29*, 453–460. [CrossRef]
36. Moreto, C.P.N.; Monteiro, L.V.S.; Xavier, R.P.; Creaser, R.A.; DuFrane, S.A.; Tassinari, C.C.G.; Sato, K.; Kemp, A.I.S.; Amaral, W.S. Neoarchean and Paleoproterozoic Iron Oxide-Copper-Gold Events at the Sossego Deposit, Carajás Province, Brazil: Re-Os and U-Pb Geochronological Evidence. *Econ. Geol.* **2015**, *110*, 809–835. [CrossRef]
37. Martins, P.L.G.; Toledo, C.L.B.; Silva, A.M.; Chemale, F.; Santos, J.O.S.; Assis, L.M. Neoarchean Magmatism in the Southeastern Amazonian Craton, Brazil: Petrography, Geochemistry and Tectonic Significance of Basalts from the Carajás Basin. *Precambrian Res.* **2017**, *302*, 340–357. [CrossRef]
38. Siepierski, L.; Ferreira Filho, C.F. Magmatic Structure and Petrology of the Vermelho Complex, Carajás Mineral Province, Brazil: Evidence for Magmatic Processes at the Lower Portion of a Mafic-Ultramafic Intrusion. *J. S. Am. Earth Sci.* **2020**, *102*, 102700. [CrossRef]
39. Rossignol, C.; Antonio, P.Y.J.; Narduzzi, F.; Rego, E.S.; Teixeira, L.; de Souza, R.A.; Ávila, J.N.; Silva, M.A.L.; Lana, C.; Trindade, R.I.F.; et al. Unraveling One Billion Years of Geological Evolution of the Southeastern Amazonia Craton from Detrital Zircon Analyses. *Geosci. Front.* **2022**, *13*, 101202. [CrossRef]
40. Pereira, M.A.M.; Moreto, C.P.N.; Dellinardo-Silva, M.A.; Melo, G.H.C.; Correa, A.I.C.M.; Sanches, J.M.; Silva, A.D.F.; Soares, M.A.M.; Costa, L.C.C.; Araújo, J. Microstructures as a Tectonic Guide to Unravel Structural Controls on Cu-Au Mineralization at the Neoarchean Pantera IOCG Deposit, Carajás Domain. In Proceedings of the Anais do XI Simpósio Brasileiro de Exploração Mineral, Ouro Preto, Brazil, 19–22 May 2024.
41. Tavares, F.M.; Trouw, R.A.J.; da Silva, C.M.G.; Justo, A.P.; Oliveira, J.K.M. The Multistage Tectonic Evolution of the Northeastern Carajás Province, Amazonian Craton, Brazil: Revealing Complex Structural Patterns. *J. S. Am. Earth Sci.* **2018**, *88*, 238–252. [CrossRef]
42. Vasquez, M.L.; Macambira, M.J.B.; Armstrong, R.A. Zircon Geochronology of Granitoids from the Western Bacajá Domain, Southeastern Amazonian Craton, Brazil: Neoarchean to Orosirian Evolution. *Precambrian Res.* **2008**, *161*, 279–302. [CrossRef]
43. Dall'Agnol, R.; Teixeira, N.P.; Rämö, O.T.; Moura, C.A.V.; Macambira, M.J.B.; de Oliveira, D.C. Petrogenesis of the Paleoproterozoic Rapakivi A-Type Granites of the Archean Carajás Metallogenic Province, Brazil. *Lithos* **2005**, *80*, 101–129. [CrossRef]
44. Bordalo, R.A.; dos Santos, T.J.S.; Dantas, E.L. Structural Evolution and U/Pb Zircon Age of the Xambioá Gneiss Dome, Contributions to the Araguaia Fold Belt Tectonic History. *J. S. Am. Earth Sci.* **2020**, *104*, 102753. [CrossRef]
45. Teixeira, W.; Hamilton, M.A.; Girardi, V.A.V.; Faleiros, F.M.; Ernst, R.E. U-Pb Baddeleyite Ages of Key Dyke Swarms in the Amazonian Craton (Carajás/Rio Maria and Rio Apa Areas): Tectonic Implications for Events at 1880, 1110 Ma, 535 Ma and 200 Ma. *Precambrian Res.* **2019**, *329*, 138–155. [CrossRef]
46. Carneiro, L.S.; Moreto, C.P.N.; Monteiro, L.V.S.; Delinardo-Silva, M.A.; Melo, G.H.C.; Xavier, R.P.; Pozocco, E.; Carvalho, J.A.; Schoenherr, I.; Oliveira, G.D.; et al. The 2.86 Ga Hades and Hades Nordeste Copper Deposits, SW Carajás: Implications for the Mesoarchean Deformation-Mineralization Processes. In *Proceedings of the 17 Simpósio de Geologia da Amazônia, Santarém, Brazil, 23–25 October 2023*; Sociedade Brasileira de Geologia: Santarém, Brazil, 2023.
47. Melo, G.H.C.; Monteiro, L.V.S.; Xavier, R.P.; Moreto, C.P.N.; Arquaz, R.M.; Silva, M.A.D. Evolution of the Igarapé Bahia Cu-Au Deposit, Carajás Province (Brazil): Early Syngenetic Chalcopyrite Overprinted by IOCG Mineralization. *Ore Geol. Rev.* **2019**, *111*, 102993. [CrossRef]

48. Xavier, R.P.; Soares Monteiro, L.V.; Moreto, C.P.N.; Pestilho, A.L.S.; Coelho de Melo, G.H.; Delinardo da Silva, M.A.; Aires, B.; Ribeiro, C.; Freitas e Silva, F.H. The Iron Oxide Copper-Gold Systems of the Carajás Mineral Province, Brazil. In *Geology and Genesis of Major Copper Deposits and Districts of the World: A Tribute to Richard H. Sillitoe*; Society of Economic Geologists: Littleton, CO, USA, 2012; Volume 16, pp. 433–454.
49. Vendemiatto, M.A.; Enzweiler, J. Routine Control of Accuracy in Silicate Rock Analysis by X-Ray Fluorescence Spectrometry. *Geostand. Newsl.* **2001**, *25*, 283–291. [CrossRef]
50. Navarro, M.S.; Andrade, S.; Ulbrich, H.; Gomes, C.B.; Girardi, V.A.V. The Direct Determination of Rare Earth Elements in Basaltic and Related Rocks Using ICP-MS: Testing the Efficiency of Microwave Oven Sample Decomposition Procedures. *Geostand. Geoanalyt. Res.* **2008**, *32*, 167–180. [CrossRef]
51. Janoušek, V.; Farrow, C.M.; Erban, V. Interpretation of Whole-Rock Geochemical Data in Igneous Geochemistry: Introducing Geochemical Data Toolkit (GCDkit). *J. Petrol.* **2006**, *47*, 1255–1259. [CrossRef]
52. Brophy, J.G.; Ota, T.; Kunihro, T.; Tsujimori, T.; Nakamura, E. In Situ Ion-Microprobe Determination of Trace Element Partition Coefficients for Hornblende, Plagioclase, Orthopyroxene, and Apatite in Equilibrium with Natural Rhyolitic Glass, Little Glass Mountain Rhyolite, California. *Am. Mineral.* **2011**, *96*, 1838–1850. [CrossRef]
53. Ewart, A.; Griffin, W.L. Application of Proton-Microprobe Data to Trace-Element Partitioning in Volcanic Rocks. *Chem. Geol.* **1994**, *117*, 251–284. [CrossRef]
54. Nash, W.P.; Crecraft, H.R. Partition Coefficients for Trace Elements in Silicic Magmas. *Geochim. Cosmochim. Acta* **1985**, *49*, 2309–2322. [CrossRef]
55. Vermeesch, P. IsoplotR: A Free and Open Toolbox for Geochronology. *Geosci. Front.* **2018**, *9*, 1479–1493. [CrossRef]
56. Mehnert, K.R. *Migmatites and the Origin of Granitic Rocks*; Elsevier Publishing Company: Amsterdam, The Netherlands, 1968.
57. Sawyer, E.W. *Atlas of Migmatites*; Canadian Science Publishing: Ottawa, ON, Canada, 2008; ISBN 9780660197883.
58. Holness, M.B. Decoding Migmatite Microstructures. In *Working with Migmatites*; Mineralogical Association of Canada: Quebec City, QC, Canada, 2008; pp. 57–76.
59. Holness, M.B.; Sawyer, E.W. On the Pseudomorphing of Melt-Filled Pores During the Crystallization of Migmatites. *J. Petrol.* **2008**, *49*, 1343–1363. [CrossRef]
60. Vernon, R.H. Microstructures of Melt-Bearing Regional Metamorphic Rocks. In *Origin and Evolution of Precambrian High-Grade Gneiss Terranes, with Special Emphasis on the Limpopo Complex of Southern Africa*; Geological Society of America: Boulder, CO, USA, 2011; Volume 207, pp. 1–11; ISBN 9780813712079.
61. Warr, L.N. IMA–CNMNC Approved Mineral Symbols. *Mineral. Mag.* **2021**, *85*, 291–320. [CrossRef]
62. McDonough, W.F.; Sun, S.S. The Composition of the Earth. *Chem. Geol.* **1995**, *120*, 223–253. [CrossRef]
63. O'Connor, J.T. A Classification for Quartz-Rich Igneous Rocks Based on Feldspar Ratios. *Geol. Surv. Prof. Pap.* **1965**, *525*, 79–84.
64. Frost, B.R.; Barnes, C.G.; Collins, W.J.; Arculus, R.J.; Ellis, D.J.; Frost, C.D. A Geochemical Classification for Granitic Rocks. *J. Petrol.* **2001**, *42*, 2033–2048. [CrossRef]
65. Shand, S.J. *Eruptive Rocks: Their Genesis, Composition, Classification and Their Relation to Ore Deposits, with a Chapter on Meteorites*, 2nd ed.; Thomas Murby and Co.: London, UK, 1943.
66. Ashworth, J.R.; Johannes, W.; Grant, J.A.; Olsen, S.N.; McLellan, E.L.; Tracy, R.J.; Barr, D.; Touret, J. *Migmatites*; Ashworth, J.R., Ed.; Springer: Boston, MA, USA, 1985; ISBN 978-1-4612-9438-2.
67. Lappin, A.R.; Hollister, L.S. Partial Melting in the Central Gneiss Complex near Prince Rupert, British Columbia. *Am. J. Sci.* **1980**, *280*, 518–545. [CrossRef]
68. Lee, Y.; Cho, M. Fluid-Present Disequilibrium Melting in Neoarchean Arc-Related Migmatites of Daeijak Island, Western Gyeonggi Massif, Korea. *Lithos* **2013**, *179*, 249–262. [CrossRef]
69. Mogk, D.W. Ductile Shearing and Migmatization at Mid-crustal Levels in an Archaean High-grade Gneiss Belt, Northern Gallatin Range, Montana, USA. *J. Metamorph. Geol.* **1992**, *10*, 427–438. [CrossRef]
70. Sawyer, E.W. Migmatites Formed by Water-Fluxed Partial Melting of a Leucogranodiorite Protolith: Microstructures in the Residual Rocks and Source of the Fluid. *Lithos* **2010**, *116*, 273–286. [CrossRef]
71. Watkins, J.M.; Clemens, J.D.; Treloar, P.J. Archaean TTGs as Sources of Younger Granitic Magmas: Melting of Sodic Metatonalites at 0.6–1.2 GPa. In *Contributions to Mineralogy and Petrology*; Springer: Berlin/Heidelberg, Germany, 2007; Volume 154, pp. 91–110. [CrossRef]
72. Weinberg, R.F.; Hasalová, P. Water-Fluxed Melting of the Continental Crust: A Review. *Lithos* **2015**, *212–215*, 158–188. [CrossRef]
73. Siepierski, L.; Ferreira Filho, C.F. Spinifex-Textured Komatiites in the South Border of the Carajas Ridge, Selva Greenstone Belt, Carajás Province, Brazil. *J. S. Am. Earth Sci.* **2016**, *66*, 41–55. [CrossRef]
74. Goldfarb, R.J.; Baker, T.; Dubé, B.; Groves, D.I.; Hart, C.J.R.; Gosselin, P. Distribution, Character, and Genesis of Gold Deposits in Metamorphic Terran. In *One Hundredth Anniversary Volume*; Society of Economic Geologists: Littleton, CO, USA, 2005; pp. 407–450.

75. do Nascimento, A.C.; de Oliveira, D.C.; da Silva, L.R.; Lamarão, C.N. Mineral Thermobarometry and Its Implications for Petrological Constraints on Mesoarchean Granitoids from the Carajás Province, Amazonian Craton (Brazil). *J. S. Am. Earth Sci.* **2021**, *109*, 103271. [CrossRef]
76. do Nascimento, A.C.; de Oliveira, D.C.; Gabriel, E.O.; Marangoanha, B.; Ribeiro da Silva, L.; da Aleixo, E.C. Mineral Chemistry of the Água Limpa Suite: Insights into Petrological Constraints and Magma Ascent Rate of Mesoarchean Sanukitoids from the Sapucaia Terrane (Carajás Province, Southeastern Amazonian Craton, Brazil). *J. S. Am. Earth Sci.* **2023**, *132*, 104683. [CrossRef]
77. Klimm, K.; Holtz, F.; Johannes, W.; King, P.L. Fractionation of Metaluminous A-Type Granites: An Experimental Study of the Wangrah Suite, Lachlan Fold Belt, Australia. *Precambrian Res.* **2003**, *124*, 327–341. [CrossRef]
78. Spencer, C.J.; Kirkland, C.L.; Taylor, R.J.M. Strategies towards Statistically Robust Interpretations of in Situ U-Pb Zircon Geochronology. *Geosci. Front.* **2016**, *7*, 581–589. [CrossRef]
79. Goodwin, L.B.; Tikoff, B. Competency Contrast, Kinematics, and the Development of Foliations and Lineations in the Crust. *J. Struct. Geol.* **2002**, *24*, 1065–1085. [CrossRef]
80. Slagstad, T.; Jamieson, R.A.; Culshaw, N.G. Formation, Crystallization, and Migration of Melt in the Mid-Orogenic Crust: Muskoka Domain Migmatites, Grenville Province, Ontario. *J. Petrol.* **2005**, *46*, 893–919. [CrossRef]
81. Guernina, S.; Sawyer, E.W. Large-scale Melt-depletion in Granulite Terranes: An Example from the Archean Ashuanipi Subprovince of Quebec. *J. Metamorph. Geol.* **2003**, *21*, 181–201. [CrossRef]
82. Hawkesworth, C.; Cawood, P.A.; Dhuime, B.; Kemp, T. Tectonic Processes and the Evolution of the Continental Crust. *J. Geol. Soc. Lond.* **2024**, *181*, jgs2024-027. [CrossRef]
83. Van Kranendonk, M.J.; Collins, W.J.; Hickman, A.H.; Powley, M.J. Critical Tests of Vertical vs. Horizontal Tectonic Models for the Archaean East Pilbara Granite–Greenstone Terrane, Pilbara Craton, Western Australia. *Precambrian Res.* **2004**, *131*, 173–211. [CrossRef]
84. Lamont, T.N.; Searle, M.P.; Waters, D.J.; Roberts, N.M.W.; Palin, R.M.; Smye, A.; Dyck, B.; Gopon, P.; Weller, O.M.; St-Onge, M.R. Compressional Origin of the Naxos Metamorphic Core Complex, Greece: Structure, Petrography, and Thermobarometry. *Bull. Geol. Soc. Am.* **2020**, *132*, 149–197. [CrossRef]
85. Kusky, T.; Windley, B.F.; Polat, A.; Wang, L.; Ning, W.; Zhong, Y. Archean Dome-and-Basin Style Structures Form during Growth and Death of Intraoceanic and Continental Margin Arcs in Accretionary Orogens. *Earth-Sci. Rev.* **2021**, *220*, 103725. [CrossRef]
86. Arndt, N. Formation and Evolution of the Continental Crust. *Geochem. Perspect.* **2013**, *2*, 405–533. [CrossRef]
87. Condie, K.C. Tectonic Settings. In *Earth as an Evolving Planetary System*; Elsevier: Amsterdam, The Netherlands, 2016; pp. 43–88, ISBN 9780128036891.
88. Touret, J.L.R.; Santosh, M.; Huizenga, J.M. Composition and Evolution of the Continental Crust: Retrospect and Prospect. *Geosci. Front.* **2022**, *13*, 101428. [CrossRef]
89. Skirrow, R.G. Iron Oxide Copper-Gold (IOCG) Deposits—A Review (Part 1): Settings, Mineralogy, Ore Geochemistry and Classification. *Ore Geol. Rev.* **2022**, *140*, 104569. [CrossRef]
90. Groves, D.I.; Bierlein, F.P.; Meinert, L.D.; Hitzman, M.W. Iron Oxide Copper-Gold (IOCG) Deposits through Earth History: Implications for Origin, Lithospheric Setting, and Distinction from Other Epigenetic Iron Oxide Deposits. *Econ. Geol.* **2010**, *105*, 641–654. [CrossRef]
91. Skirrow, R.G.; van der Wielen, S.E.; Champion, D.C.; Czarnota, K.; Thiel, S. Lithospheric Architecture and Mantle Metasomatism Linked to Iron Oxide Cu-Au Ore Formation: Multidisciplinary Evidence from the Olympic Dam Region, South Australia. *Geochem. Geophys. Geosystems* **2018**, *19*, 2673–2705. [CrossRef]
92. McPhie, J.; DellaPasqua, F.; Allen, S.R.; Lackie, M.A. Extreme Effusive Eruptions: Palaeoflow Data on an Extensive Felsic Lava in the Mesoproterozoic Gawler Range Volcanics. *J. Volcanol. Geotherm. Res.* **2008**, *172*, 148–161. [CrossRef]
93. Jagodzinski, E.A.; Reid, A.J.; Crowley, J.L.; Wade, C.E.; Curtis, S. Precise Zircon U-Pb Dating of the Mesoproterozoic Gawler Large Igneous Province, South Australia. *Results Geochem.* **2023**, *10*, 100020. [CrossRef]